Impact of Zn Substitution on Fe(II)-induced Ferrihydrite Transformation Pathways

Jinshu Yan[1], Andrew J. Frierdich[2], and Jeffrey G. Catalano[1*]

1. Department of Earth and Planetary Sciences, Washington University in St. Louis, Saint Louis, MO 63130, USA

2. School of Earth, Atmosphere & Environment, Monash University, Clayton, VIC 3800, Australia

*Corresponding author: Email: catalano@wustl.edu, Twitter handle: @jeff_catalano

Submitted to *Geochimica et Cosmochimica Acta*
July 2021

ABSTRACT

Iron oxide minerals are ubiquitous in soils, sediments, and aquatic systems and influence the fate and availability of trace metals. Ferrihydrite is a common iron oxide of nanoparticulate size and poor crystallinity, serving as a thermodynamically unstable precursor to more crystalline phases. While aging induces such phase transformations, these are accelerated by the presence of dissolved Fe(II). However, the impact of trace metals on Fe(II)-catalyzed ferrihydrite phase transformations at ambient temperatures and the associated effects on trace metal speciation has seen limited study. In the present work, phase transformations of ferrihydrite that contains the trace metal zinc in its structure were investigated during aging at ambient temperature in the presence of two different Fe(II) concentrations at pH 7. X-ray diffraction reveals that low Fe(II) concentration (0.2 mM) generates hematite plus minor lepidocrocite, whereas high Fe(II) concentration (1.0 mM) promotes the production of a magnetite-lepidocrocite mixture. In both cases, a substantial fraction of ferrihydrite remains after 12 days. In contrast, Zn-free ferrihydrite forms primarily lepidocrocite and goethite in the presence of 0.2 mM Fe(II), with minor hematite and a trace of ferrihydrite remaining. For 1.0 mM Fe(II), magnetite, goethite, and lepidocrocite form when Zn is absent, leaving no residual ferrihydrite. Transformations of Zn-ferrihydrite produce a transient release of zinc to solution, but this is nearly quantitatively removed into the mineral products after 1 hour. Extended X-ray absorption fine structure spectroscopy suggests that zinc partitions into the newly formed phases, with a shift from tetrahedral to a mixture of tetrahedral and octahedral coordination in the 0.2 mM Fe(II) system and taking on a spinel-like local structure in the 1.0 mM Fe(II) reaction products. This work indicates that substituting elements in ferrihydrite may play a key role in promoting the formation of hematite in low temperature systems, such as soils or sediments. In addition, the retention of zinc in the products

of ferrihydrite phase transformation shows that trace metal micronutrients and contaminants may not be mobilized under circumneutral conditions despite the formation of more crystalline iron oxides. Furthermore, mass balance requires that the abundance and isotopic composition of iron oxide-associated zinc, and possibly other trace metals, in the rock record may be retained during diagenetic phase transformations of ferrihydrite if catalyzed by dissolved Fe(II).

1. INTRODUCTION

Ferrihydrite is a ubiquitous, naturally occurring iron oxide that is commonly found in soils and aquatic environments (Combes et al., 1990; Jambor and Dutrizac, 1998; Cornell and Schwertmann, 2003). It has high surface area and is nanocrystalline, producing greater reactivity compared to other iron oxides (Hiemstra, 2013; Hiemstra, 2015). The fate and transport of metal ions is often controlled by sorption to ferrihydrite and other iron oxide minerals (Brown and Parks, 2001; Scheinost et al., 2001; Manceau et al., 2007; Gustafsson et al., 2011; Eickhoff et al., 2014; Tian et al., 2017). Aging of metals sorbed to ferrihydrite enhances their retention, possibly through incorporation (Schultz et al., 1987; Ainsworth et al., 1994; Ford et al., 1997). In addition, metals present during ferrihydrite formation may coprecipitate into the mineral structure (Martínez and McBride, 1998; Ford et al., 1999; Dai et al., 2017).

Ferrihydrite is thermodynamically unstable with respect to other more crystalline iron oxides such as lepidocrocite, goethite, and hematite (Navrotsky et al., 2008), and transforms over time to these more stable phases (Schwertmann and Taylor, 1972; Cornell and Schwertmann, 2003). Such transformations play essential roles in determining iron oxide mineralogy in soils (Kämpf and Schwertmann, 1983; Nørnberg et al., 2009; Jiang et al., 2018) as well as modern and ancient sedimentary systems (Chan et al., 2007; Bekker et al., 2010). Ferrihydrite phase transformations involve competitive processes influenced by various factors, such as temperature, ligand type, and pH (Fischer and Schwertmann, 1975; Schwertmann et al., 1999; Cornell and Schwertmann, 2003). Hematite formation from a ferrihydrite precursor occurs rapidly at temperatures of 50 to 100°C (Fischer and Schwertmann, 1975; Johnston and Lewis, 1983; Liu et al., 2005; Das et al., 2011; Soltis et al., 2016; Jiang et al., 2018) but at 4 to 30°C requires years of aging (Schwertmann and Murad, 1983; Schwertmann et al., 1999; Schwertmann et al., 2000b; Schwertmann et al., 2000a; Schwertmann et al., 2004; Das et al., 2011). Goethite is promoted over hematite at cooler temperature, higher humidity, and at either acidic or alkaline pH (Torrent et al., 1982; Schwertmann and Murad, 1983; Nagano et al., 1994; Das et al., 2011; Zhang et al., 2018).

Ferrihydrite transformation to more crystalline phases can be rapidly induced by dissolved Fe(II). At ambient temperatures, this process yields lepidocrocite, goethite, and, at elevated Fe(II) concentrations, magnetite (Tronc et al., 1992; Hansel et al., 2003; Hansel et al., 2005; Pedersen et al., 2005; Yee et al., 2006; Liu et al., 2007; Yang et al., 2010; Hansel et al., 2011; Boland et al., 2013; Boland et al., 2014; Liu et al., 2016; Tomaszewski et al., 2016; Jones et al., 2017). Hematite also occurs when ferrihydrite reacts with dissolved Fe(II) at elevated temperature, typically 60 °C or greater (Hansel et al., 2005; Liu et al., 2005; Pedersen et al., 2005; Liu et al., 2008; Wang et al., 2015). Fe(II) catalyzed transformations to goethite and lepidocrocite involve adsorption and electron transfer at the mineral surface, producing a reactive Fe(III) species that facilitates mass transfer, growth, and formation of new phases (Boland et al., 2014; Sheng et al., 2020b). Ligand type impacts ferrihydrite transformation pathways: chloride favors the transformation of ferrihydrite to lepidocrocite, while sulfate supports the conversion to both goethite and lepidocrocite (Hansel et al., 2005; Liu et al., 2008). pH variations affect the formation of magnetite, the relative amounts of goethite and lepidocrocite produced, and the rate of ferrihydrite transformation (Hansel et al., 2005; Boland et al., 2014). Surface adsorbates, including silicate and organic matter, both slow ferrihydrite transformation and alter the final minerals that form (Jones et al., 2009; Wang et al., 2015; Thomasarrigo et al., 2018; Xiao et al., 2018; Zhou et al., 2018; Thomasarrigo et al., 2019; Sheng et al., 2020a). Aluminum substitution diminishes secondary mineralization and enhances preservation of ferrihydrite, requiring greater Fe(II) concentrations to induce transformation compared to Al-free ferrihydrite (Masue-Slowey et al., 2011; Hansel et al., 2011).

Trace metals also impact ferrihydrite transformations. At 70°C, coprecipitated divalent metal cations may either promote or inhibit ferrihydrite transformation in Fe(II)-free systems (Cornell, 1988; Martínez and McBride, 1998). Dissolved Zn alters thermal transformation products of ferrihydrite at 70°C, increasing hematite content at the expense of goethite through a Zn-maghemite precursor while also forming franklinite because of the high Zn concentrations used (Sakakibara et al., 2019). At ambient temperature, adsorbed divalent cations (Liu et al., 2016) or rare earth elements (Fei et al., 2018) inhibit Fe(II)-catalyzed ferrihydrite transformations and alter the amounts of goethite, lepidocrocite, and magnetite that formed. No prior studies have reported that metals promote hematite formation near 25°C or cooler.

Despite the extensive study of ferrihydrite conversion to other minerals, the role of incorporated trace metals in affecting Fe(II)-catalyzed ferrihydrite transformations and the resulting fate of such metals is poorly understood at ambient temperatures. This study thus investigates the behavior of Zn during Fe(II)-induced ferrihydrite transformations at 22°C. Batch aging experiments were carried out in which Zn-substituted ferrihydrite was exposed to 0.2 mM or 1.0 mM dissolved Fe(II) at pH 7 for 12 days. X-ray diffraction (XRD) patterns collected over the course of the experiment tracked the mineralogical evolution, with mineral abundances quantified via Rietveld refinement. Concentrations of dissolved Zn and Fe were measured over time to study the release and uptake of Zn as well as the consumption and adsorption of Fe(II). X-ray absorption fine structure (XAFS) spectra were obtained to evaluate the coordination state of Zn associated with iron oxide minerals at different aging times.

2. MATERIALS AND METHODS

2.1. Mineral Synthesis

Zn-substituted ferrihydrite was synthesized using a modification of previously described methods for the 2-line form of this mineral (Schwertmann and Cornell, 2000). 73.5 mL of 5 M sodium hydroxide was added dropwise over 20 minutes into a 125 mL solution containing 0.98 M ferric nitrate and 0.02 M zinc chloride that was continuously stirred. Solution pH was continuously measured and maintained below pH 11, as high pH favors the formation of goethite. The resulting suspension was then centrifuged at 15000 rpm for 20 minutes. After centrifugation, the majority of the supernatant was decanted off, and the precipitate was resuspended in ultrapure water (>18.2 MΩ cm) and then centrifuged again. This process was repeated 6 times until the particles would no longer settle during centrifugation, indicating a substantial decrease in ionic strength. After the final centrifugation, ferrihydrite was resuspended in ultrapure water; the pH of this suspension was 6.9. The suspension was then freeze dried and stored in polypropylene bottles wrapped in aluminum foil at room temperature. The drying step was done to inhibit changes in ferrihydrite properties associated with aging as a suspension (Hiemstra et al., 2019) and to maintain a single batch of Zn-substituted ferrihydrite for use in multiple experiments. Zn-free ferrihydrite was prepared using the same procedure but with the initial 125 mL solution containing 1.0 M ferric nitrate and no added zinc chloride.

2.2. Mineral Transformation Experiments

All solutions were prepared in an anaerobic chamber (Coy Laboratory Products) in a ~3% H_2 and ~97% N_2 atmosphere that was circulated over a Pd catalyst to eliminate residual O_2. Ultrapure water was deoxygenated by bubbling for at least 5 hours with ultrahigh purity N_2 (<1 ppmv O_2) before being transferred into the glove box. The oxygen level in the deoxygenated ultrapure water was further lowered by sparging with anaerobic chamber atmosphere that was first bubbled through a 10% pyrogallol/40% potassium hydroxide solution, which serves as a secondary oxygen trap that also scavenges CO_2. Dissolved oxygen was measured colorimetrically using CHEMets test kit K-7540 to confirm a concentration below the ~1 μg/L detection limit. Synthesized ferrihydrite with and without structural Zn was brought into the glove box at least 48 hours prior to use. All salts used were ACS reagent grade or better and were prepared in the anaerobic chamber as stock solutions.

Experiments were conducted in solutions containing final concentrations of 10^{-2} M sodium chloride, 10^{-3} M 3-(N-Morpholino) propanesulfonic acid (MOPS, a pH buffer with a pKa value of 7.20), and either 1.0 mM or 0.2 mM dissolved Fe(II), prepared from iron(II) chloride tetrahydrate. The initial pH was adjusted to 7.0 using 0.1 N NaOH and 0.1 N HCl. A Zn-substituted ferrihydrite suspension was prepared at an initial concentration of 4 g/L of ground, freeze-dried ferrihydrite in deoxygenated deionized water. A desired volume of the suspension was injected into to the sample solution to reach a final concentration of 1 g/L. Addition of Zn-ferrihydrite marked the start of the reaction. Each experiment was conducted in a 500 mL polypropylene bottle with the fluid continuously stirred using a magnetic stirrer with a PTFE-coated magnet. The bottle was wrapped in aluminum foil to inhibit photoreduction and the cap was sealed using vinyl tape to decrease the possibility of residual oxygen in the anaerobic chamber from inadvertently oxidizing the solution.

The pH of the solution was checked, recorded, and adjusted back to 7.00±0.05 daily during the reaction. 20 mL subsamples of the well-mixed suspension were removed after 2 minutes, 5 minutes, 15 minutes, 1 hour, 2 hours, 4 hours, 7 hours, 1 day, 3 days, 5 days, 7 days, and 12 days. Each was immediately filtered using a 0.22 μm mixed cellulose ester (MCE) membrane in a polypropylene syringe filter enclosure. Ferrihydrite aggregation was adequate to allow separation of particles from the fluid via filtration as confirmed by the lack of dissolved Fe measured in Fe(II)-free control samples. Duplicates were collected on days 7 and 12 to assess the reproducibility of the measurements. The filtered fluids were then removed from the anaerobic chamber and acidified with 2% trace meal grade nitric acid before dissolved Fe and Zn concentrations were measure by inductively-coupled plasma mass spectrometry (ICP-MS) using a Thermo iCAP Q instrument. Minerals collected on the filter membranes were dried in a vacuum desiccator inside the anaerobic chamber for further characterization.

A set of control experiments were carried out in separate tubes to evaluate possible sources of experimental error and to assess the impact of dissolved Fe(II) and substituting Zn on the reactions. Two control experiments were prepared with the same fluid composition as described above (one for each Fe(II) concentration) but no minerals were added in order to evaluate possible sample contamination with Zn, as has been noted in prior work (Kay, 2004; Bryan et al., 2015; Garçon et al., 2017). Two additional control experiments (again, one for each Fe(II) concentration) replicated the studies described above by added Zn-free ferrihydrite instead of Zn-substituted ferrihydrite. Mineral and filtered fluid samples were collected after 12 days of reaction for these control experiments.

2.3 Mineral characterization

Mineral solids were analyzed by powder X-ray diffraction (XRD) using a Bruker d8 Advance diffractometer equipped with a Cu X-ray tube operating at 40 kV and 40 mA. The initial synthetic ferrihydrite samples and the solids collected after select reaction times were studied. Minerals were ground using an agate mortar and pestle and mounted on a zero-background silicon sample holder. XRD scans were performed from 15° to 85° with a 0.02° step-size, 0.5 s count time per step at a rotation rate of 15 rotations per minute. A LynxEye XE energy-dispersive silicon-strip detector was used for data collection in a continuous scan mode, with each of the 192 detector strips measuring the same angular position for the specified counting time. This yielded a total integration time of 96 s per 2θ value. The Diffrac.Eva application was used for initial phase identification. Rietveld refinement of the XRD patterns determined the quantitative abundances of crystalline phases and the semi-quantitative abundance of ferrihydrite using a partially empirical approach (see Electronic Annex). Fitting was conducted in the Profex (Doebelin and Kleeberg, 2015) interface to BGMN (Bergmann et al., 1998). Brunauer-Emmett-Teller (BET) specific surface area of each synthesized mineral was determined by collecting N_2 gas adsorption isotherms using a Quantachrome Autosorb-1 Instrument. The Zn concentration in Zn-substituted ferrihydrite was determined by acid digestion. 5 mg of ferrihydrite was dissolved in 10 mL of 4 M hydrochloric acid at 70°C. The solution was then diluted 1:100 using 2% trace metal grade nitric acid and measured by ICP-MS.

2.4 X-ray absorption fine structure spectroscopy

Zn K-edge XAFS spectra, including the X-ray absorption near-edge structures (XANES) and extended X-ray absorption fine-structure (EXAFS) regions, were measured on the initial Zn-ferrihydrite, a Zn-hematite standard, and the solid-phase products formed from reaction of Zn-ferrihydrite with 0.2 mM Fe(II) for 2 h and 12 d with 1.0 mM Fe(II) after 12 days. Preparation of the Zn-hematite standard was described in a prior study (Frierdich et al., 2012). Data collection was performed on beamline 12-BM-B at the Advanced Photon Source (APS) at Argonne National Laboratory. The beamline employed a Si (111) fixed offset monochromator which was detuned 30% to reduce the harmonic content of the beam. Toroidal focusing and flat mirrors were used to increase usable X-ray flux and further reduce harmonics, with focusing effects resulting in a beam of ~700 µm diameter. Zn K-edge data were collected in fluorescence yield with a 13-element energy-dispersive Ge detector. Aluminum foil was used to selectively reduce the Fe fluorescence intensity in order to prevent detector saturation. An additional standard of Zn adsorbed to hematite was prepared by reacting 0.2 mM zinc chloride with 4 g L^{-1} synthetic hematite in a 0.01 M sodium chloride solution for 5 days at pH 7.5. Details of the hematite synthesis and sample preparation follow procedures described previously (Frierdich et al., 2011). The Zn K-edge XAFS spectrum of this additional sample was measured at APS beamline 20-BM-B using similar optics and detector details as those described above.

The X-ray energy for all measurements was calibrated by setting the maximum in the first derivative of the X-ray absorption near-edge structure spectrum of a Zn metal foil to 9659 eV for the Zn K-edge. XAFS spectral scans were averaged using the Athena (Ravel and Newville, 2005) interface to IFEFFIT (Newville, 2001). The normalized and background subtracted k^3-weighted EXAFS spectra of Zn were fitted to structural models in SixPACK (Webb, 2005) using phase and amplitude functions generated from the structure of franklinite (Verwey and Heilmann, 1947) using FEFF 7.02 (Ankudinov and Ravel, 1998). Spectra were fit in *k*-space over a range of 3.0 to 11.3 Å and in R-space from 1.0 to 4.0 Å for all samples and standards. The coordination number

(N), interatomic distances (R), σ^2 (a Debye−Waller-type factor based on a Guassian distribution of interatomic distances), and ΔE_0 were refined using nonlinear least-squares fitting. The amplitude reduction factor (S_0^2) was fixed at 0.9 for spectral fitting. Linear combination fitting in select cases was conducted in Athena.

3. RESULTS

3.1 Characterization of Zn-ferrihydrite and Zn-free Ferrihydrite

XRD reveals that Zn-ferrihydrite contained no detectable crystalline impurities, yielding a pattern consistent with that of 2-line ferrihydrite (Fig. 1a). Zn-free ferrihydrite generated an XRD pattern indistinguishable from the Zn-substituted phase. The Zn content of the substituted ferrihydrite determined by acid digestion was 2.2 mol.%, close to the target substitution level of 2.0 mol.%. The BET specific surface areas for Zn-free ferrihydrite and Zn-ferrihydrite are 297 m^2/g and 233 m^2/g, respectively. Structural analysis of the Zn K-edge EXAFS spectrum (Fig. 1b) of Zn-ferrihydrite shows that Zn substitutes in tetrahedral configuration, as indicated by the Zn-O interatomic distance and coordination number (Table 1). The Zn-Fe distance of ~3.45 Å (Table 1) indicates corner-sharing between a zinc tetrahedron and an iron octahedron, a geometry also consistent with zinc substituting into the proposed tetrahedral iron site in ferrihydrite (Michel et al., 2007; Michel et al., 2010; Maillot et al., 2011).

3.2 Phase Transformations of Zn-ferrihydrite

3.2.1 Transformations in 0.2 mM Fe(II)

Upon contact with 0.2 mM dissolved Fe(II), Zn-ferrihydrite showed no evidence of converting to more crystalline phases over the first few hours of reaction (Fig. 2). By 1 d of reaction, initial hematite peaks appeared in the XRD pattern, with both hematite and lepidocrocite clearly present after 3 d of reaction. These continued to grow in through the 12 d duration of the experiment (Fig. 2). The broad ferrihydrite peaks persisted throughout much of the reaction, with weak background features present at ~35° and ~63° 2θ. Rietveld refinement of the XRD data (Fig. S2) quantified the crystalline phases formed and provided a semi-quantitative estimate of ferrihydrite abundance (Fig. 3) using an empirical approach described in the Electronic Annex. This analysis shows that hematite was the dominant crystalline product formed from Zn-ferrihydrite over the course of reaction, with lepidocrocite present as 10-20 wt.% of the crystalline phases. Ferrihydrite transformed slowly and only partially converted to crystalline phases after 12 d of reaction, with more than 50 wt.% of the initial ferrihydrite remaining (Fig. 3).

3.2.2 Transformations in 1.0 mM Fe(II)

In a 1.0 mM Fe(II) solution, Zn-ferrihydrite transforms more rapidly (Fig. 2). After 2 h of reaction, the first time point sampled, substantial lepidocrocite peaks are present. Magnetite peaks appear in the XRD pattern after 1 d and become substantial components after 3 d of reaction. The relative peak intensities of lepidocrocite and magnetite are stable between 5 and 12 d of reaction. Similar to the 0.2 mM Fe(II) experiment, the data continued to have a background feature near ~35° 2θ, suggesting that some ferrihydrite remained unreacted. Rietveld refinement of the XRD data (Fig. S3) confirms that lepidocrocite dominated the crystalline products over the first day of reaction but this evolved to a subequal mixture with magnetite that appeared to stabilize in relative proportions by 5 d of reaction (Fig. 4). While Zn-ferrihydrite transformation was more rapid compared to the 0.2 mM Fe(II) experiment, a substantial residual component (~35 wt.%) remained after 12 d (Fig. 4).

3.2.3 Control Experiments

Control experiments were conducted to evaluate the role of Zn and Fe(II) in generating the observed mineral products (Fig. 5). Aging Zn-ferrihydrite for 12 d in the absence of dissolved Fe(II) yielded no detectable phase transformation, with the XRD pattern preserving the features of 2-line ferrihydrite (Fig. 5). Zn-free ferrihydrite reacted with 0.2 mM dissolved Fe(II) for 12 d produced substantial lepidocrocite and goethite peaks and minor hematite peaks in the XRD pattern (Fig. 5). Notably, goethite was absent in the Zn-ferrihydrite experiment under the same conditions and aging time (Fig. 2). Full-pattern fitting via Rietveld refinement (Fig. S4) required a mixture of lepidocrocite, goethite, and hematite to reproduce the data. This showed that the crystalline products contained ~35 wt.% goethite, which did not form when the starting solid was Zn-ferrihydrite. The lepidocrocite content of the crystalline phases was also substantially increased for Zn-free ferrihydrite. In addition, hematite was only ~25 wt.% of the crystalline fraction of the solids compared to >80 wt.% of the crystalline phases in the Zn-ferrihydrite experiment. Only ~10 wt.% ferrihydrite remained after reaction, compared to >50 wt.% for Zn-ferrihydrite.

Reaction of Zn-free ferrihydrite with 1.0 mM dissolved Fe(II) for 12 d also produced distinct mineralogy compared to Zn-ferrihydrite. While a mixture of magnetite and lepidocrocite still formed, goethite was also present, similar to the 0.2 mM Fe(II) control experiment. Magnetite abundance was ~50 wt.% of the crystalline products, approximately the same percentage as in the Zn-ferrihydrite experiment, but less lepidocrocite formed at the expense of goethite (Fig. 3). Ferrihydrite was below detection limit, producing greater conversion of Zn-free ferrihydrite compared to Zn-ferrihydrite.

3.3 Zn Release and Uptake during Phase Transformations

3.3.1 Transformations in 0.2 mM Fe(II)

Zinc release and uptake and the removal of dissolved iron were monitored during the transformation of Zn-ferrihydrite in the presence of 0.2 mM Fe(II). At the beginning of the reaction, Zn is rapidly released to solution, with a dissolved concentration of ~20 μM Zn at the first time point (Fig. 6A). Zn was then progressively taken up into the solid phase, with near-complete removal of Zn initially released to the fluid. On the third day, Zn concentration reaches the lowest value of 0.7 μM and then gradually increased to 2 μM by the end of the 12 d experiment. The residual dissolved Zn consists of only 1% of the total Zn in the system, indicating that 99% is retained in the solid phase during phase transformation after the brief transient release during the first few minutes of reaction. The dissolved Fe concentration (Fig. 6B) similarly decreases rapidly at the beginning of the reaction and then gradually increased from day 3 to 12. The final dissolved Fe concentration was 27 μM, indicating that >86% of the initial dissolved Fe(II) was bound to the solid phase.

3.3.2 Transformations in 1.0 mM Fe(II)

The concentrations of dissolved Zn and Fe for Zn-ferrihydrite in contact with an initial 1.0 mM Fe(II) solution (Fig. 6C,D) follow patterns similar to the experiment with lower Fe(II) concentration (Fig. 6A,B). At the beginning of the reaction, ~22 μM Zn was rapidly released from Zn-ferrihydrite. Within one day, the dissolved Zn concentration displayed a drastic drop. After the third day of reaction, Zn concentration in the solution was ~7 μM, which is 3% of the initial Zn concentration. More than 97% of Zn was retained in the solid phase.

The dissolved Fe concentration experienced a sharp drop during the first hour of reaction followed by a slower decline to less than 10 μM by day 5, with >99% of the initial dissolved Fe(II) partitioning into the solid phase. During the period of large declines in dissolved Fe(II) concentration, the pH drifted down from pH 7.0 to as low as 6.6, despite the presence of a buffer in the experiment. At each sampling point the pH was thus manually adjusted to back to 7.0±0.1 by dropwise addition of 0.1 M NaOH (Fig. S5). This adjustment was performed after removal of an aliquot of the suspension for fluid and solid-phase analyses.

3.3.3 Control Experiments

Control experiments were carried out in parallel to both 0.2 mM and 1.0 mM Fe(II) experiments to further ensure the accuracy of the studies involving dissolved Fe(II) and to help interpret the results. In control sample with 10^{-2} M NaCl, 10^{-3} M MOPS, 0.2 mM Fe(II) and no mineral addition, the Zn concentration measured after 12 d of aging was 0.03 μM, indicating that Zn contamination was not a substantial contributor to the observed results. The total dissolved Fe concentration was 144 μM after 12 d, suggesting that either a portion of the Fe(II) adsorbed to the reactor walls or was oxidized, although this concentration was substantially greater than the final concentration in the corresponding experiment with Zn-ferrihydrite. In a control sample with 10^{-2} M NaCl, 10^{-3} M MOPS, 1.0 mM Fe(II) and no mineral addition, the dissolved Zn concentration was 0.31 μM after 12 d. While lower in concentration that the final Zn concentration in the experiment with Zn-ferrihydrite, it does suggest a minor source of contamination, possibly from trace amounts of Zn in the salts used. The dissolved Fe concentration after 12 d was 984 μM, suggesting negligible adsorption or oxidation occurred.

3.4 Spectroscopic Characterization of Zn

The interaction of Zn with ferrihydrite during phase transformation can be inferred from the structural information provided by EXAFS spectroscopy. Zn has various coordination states, with tetrahedral and octahedral Zn most common (Waychunas et al., 2002). Previous studies have reported that Zn(II) adsorbs on ferrihydrite as a tetrahedral complex, maintaining this geometry but with a greater number of Fe neighbors when coprecipitated (Waychunas et al., 2002; Juillot et al., 2008). In contrast, dissolved Zn(II) is octahedrally coordinated and surface complexes on hematite and goethite occur as both tetrahedral and octahedral species (Juillot et al., 2008; Ha et al., 2009). Zn substitutes into hematite and goethite as octahedral species, although these may be substantially distorted (Frierdich and Catalano, 2012; Bylaska et al., 2019). These observations are noted as they guide the structural model fitting approach used in this study.

The EXAFS spectra show that Zn coordination changes substantially during Fe(II)-catalyzed phase transformations of ferrihydrite (Fig. 7). During transformations induced by 0.2 mM Fe(II), the EXAFS spectrum of a sample collected after 2 h show little variation from the initial unreacted Zn-ferrihydrite (Fig. 7). Structural analysis confirms that Zn coordination does not detectably change over this time period (Table 1). In contrast, after 12 d of reaction with 0.2 mM Fe(II) the EXAFS spectrum is clearly different from the initial Zn-ferrihydrite. Spectral fitting (Table 1) show that a mixture of octahedral and tetrahedral Zn is present and a second Zn-Fe distance occurs at 2.97 Å. In addition, the longer Zn-Fe distance shortens slightly to 3.40 Å. These distances are similar to those observed for Zn substituting into hematite (Table 1), the dominant ferrihydrite transformation product in the sample. Visually, the EXAFS spectrum of the 12 d sample displays some muted features potentially similar to Zn in hematite, including a shift to lower *k* of the maxima near 4 Å^{-1} and two apparent oscillations between 7 and 9 Å^{-1}.

However, Zn incorporation into hematite alone does not fully explain its speciation in the 12 d sample. Linear-combination fitting well reproduces the spectrum of Zn-ferrihydrite reacted with 0.2 mM Fe(II) for 12 d using the spectra of Zn-ferrihydrite, Zn-hematite, and Zn adsorbed to hematite (see the Electronic Annex for structural analysis of the hematite standards). This analysis indicates that a large fraction of the Zn (~75%) is either incorporated into hematite or occurs in an adsorbed form, with ~25% retained in ferrihydrite. However, the resulting low component sum (0.94) suggests that the spectral standards are not fully adequate. We attribute this to possible mixtures of tetrahedral and octahedral surface complexes (Ha et al., 2009) not well represented by the Zn adsorption to hematite standard. In addition, this analysis does not account for the minor lepidocrocite component present in the mineral assemblage. Despite these minor discrepancies, the structural analysis and linear combination fitting both indicate that a substantial fraction of Zn has redistributed from ferrihydrite to hematite and likely occurs in both incorporated and adsorbed forms.

Reaction of Zn-ferrihydrite with 1.0 mM Fe(II) for 12 d produces more substantial changes in the EXAFS spectrum of Zn (Fig. 8). Notably, the spectrum has similar fine-structure as the spectrum of franklinite, but with weaker oscillations. Structural model fitting (Table 1) is consistent with Zn occupying a tetrahedral site in a ferrite spinel structure. For example, Zn in franklinite has 4 oxygen neighbors at 1.98 Å and 12 iron neighbors at 3.50 Å(Pavese et al., 2000) and the tetrahedral site in magnetite has 12 iron neighbors at 3.48 Å (Fleet, 1981). Zn likely occurs as a substituting element in the abundant magnetite produced in this reaction because franklinite was not detected via XRD (Fig. 2). Linear-combination fitting reproduces the data well with a mixture of franklinite and Zn-ferrihydrite (Fig. 8). However, some features are offset in *k*, consistent with the effects on EXAFS spectra of slight differences in interatomic distances between franklinite and magnetite. This analysis does not account for an Zn adsorbed to magnetite or associated with lepidocrocite. However, the EXAFS data clearly indicate that Zn partitions into ferrihydrite transformation products at the higher Fe(II) concentration present in this experiment.

4. DISCUSSION

4.1 Impact of Fe(II) Concentration on Ferrihydrite Transformation Pathways

Multiple prior studies demonstrate that Fe(II) concentration determines whether Fe(II) acts as a catalyst or reactant during ferrihydrite phase transformations (Tronc et al., 1992; Hansel et al., 2003; Hansel et al., 2005; Pedersen et al., 2005; Yang et al., 2010; Boland et al., 2014). In general, Fe(II) concentrations below approximately 0.4 mM favor the catalysis of ferrihydrite conversion to more crystalline Fe(III) (oxyhyd)roxides, including goethite and lepidocrocite (Yee et al., 2006; Liu et al., 2007), while at higher concentrations Fe(II) is consumed to also generate magnetite (Hansel et al., 2003; Hansel et al., 2005; Pedersen et al., 2005; Yang et al., 2010). The Fe(II) concentration needed to generate magnetite varies among different studies and is likely impacted by pH, ferrihydrite concentration, the anions present, and other factors. Our studies are consistent with past experiments, finding that 0.2 mM dissolved Fe(II) initiates only catalytic transformations, with all products consisting of ferric iron minerals. The higher concentration explored, 1.0 mM, generated substantial magnetite via reaction between Fe(II) and ferrihydrite. Note that while the fractional abundance of crystalline products of Zn-ferrihydrite transformation was dominated by lepidocrocite at early times, the absolute abundance (Table S1) increases to 37±3 wt.% after 1 d before stabilizing at 32±3 wt.% by 12 d. There thus appear to be little to no lepidocrocite conversion to magnetite; lepidocrocite simply forms first with ample Zn-ferrihydrite remaining. The absolute abundance of lepidocrocite at 1 d is affected by the amount of ferrihydrite identified using our semi-quantitative method via Rietveld refinement, and the potential small decline in absolute lepidocrocite abundance over time may reflect systematic errors in the analysis rather than real changes in mineralogy.

4.2 Impact of Zinc on Ferrihydrite Transformation Pathways

4.2.1 Promotion of Low-Temperature Hematite Formation

While hematite is the most thermodynamically stable phase among the common iron oxides in aqueous environments, its formation from ferrihydrite at ambient temperatures is slow (Cornell and Schwertmann, 2003) and the addition of Fe(II) under such conditions is not reported to produce this phase on timescales up to 9 days. Ferrihydrite stored in water over a large range of pH values (2 to 12) at temperatures of 4 to 30 °C converted to hematite after 9.3 to 12.6 years (Schwertmann et al., 1999), with hematite first apparent at 25 °C after 100s of days at pH 7 (Das et al., 2011). Hematite can also be produced at short timescales by heating ferrihydrite in water at elevated temperatures (Johnston and Lewis, 1983; Das et al., 2011). In addition, hematite was generated after heating ferrihydrite for 180 days at 45 °C and 55 °C at a relative humidity of nearly 100% (Torrent et al., 1982). This demonstrates that ferrihydrite to hematite conversion is kinetically slow without a catalyst present or thermal input. While catalytic ferrihydrite transformations induced by Fe(II) have not been reported to produce hematite at ambient temperatures (Hansel et al., 2003; Hansel et al., 2005; Pedersen et al., 2005; Lee et al., 2006; Boland et al., 2014), this product is observed for Fe(II)-ferrihydrite systems when heated at 60°C to 100°C (Liu et al., 2005; Liu et al., 2007; Liu et al., 2008).

In contrast to prior work, the present study observed rapid hematite formation from Zn-substituted 2-line ferrihydrite at room temperature (22 °C) at pH 7. Hematite clearly nucleated within three days of reaction, with the first signs of hematite in XRD patterns possibly present after one day. In addition, hematite was the dominant (>80%) crystalline product throughout the reaction. The rapid and pervasive formation of hematite is clearly related to the presence of substituting Zn as only minor hematite formed in the Zn-free control study. The promotion of hematite by Zn has been previously demonstrated in a recent thermal transformation study conducted at 70°C (Sakakibara et al., 2019). However, the present study is the first to document that Zn promotes rapid hematite formation from ferrihydrite at ambient temperatures.

4.2.2. Inhibition of Goethite Formation

Zinc also appears to inhibit goethite formation during Fe(II)-promoted ferrihydrite transformation. This phase was absent in studies of Zn-ferrihydrite but was a substantial crystalline product in the Zn-free control experiments. The formation of substantial goethite from Zn-free ferrihydrite in 0.2 mM Fe(II) was accompanied by greater lepidocrocite formation than in the Zn-ferrihydrite studies. In contrast, more goethite forms from Zn-free ferrihydrite at the apparent expense of lepidocrocite in 1.0 mM Fe(II). Zinc does not clearly affect the formation of magnetite, with similar amounts forming from Zn-ferrihydrite and Zn-free ferrihydrite. This demonstrates that Zn affects crystallization pathways beyond promoting hematite formation.

4.2.3. Inhibition of Ferrihydrite Transformation

Zinc also slows ferrihydrite transformation, leaving a substantial residual ferrihydrite pool after 12 d. Prior work suggests that a surface competition mechanism may play a role in inhibiting transformation. Adsorption of metals of higher binding affinities than Fe(II), such as Zn(II), slow the transformation rate of ferrihydrite by obstructing the Fe(II) binding to the surface (Liu et al., 2016). The release of metals from the goethite and hematite structures is also affected by the relative adsorption affinity of Fe(II) and the metal ion, which was attributed to reduced rates of recrystallization when metals are present (Frierdich and Catalano, 2012). The transient release of Zn in our study and its re-adsorption on mineral surfaces may thus hinder further transformation of ferrihydrite.

4.3 Processes Controlling Dissolved Zn and Fe Concentrations

At the beginning of the low Fe(II) (0.2 mM) transformation experiment, Zn is transiently released into the solution. This may have been caused by rapid displacement of near-surface Zn by the adsorption of Fe(II), which also showed a rapid initial decline. Fe(II) uptake continued during the initial stages of the reaction through the third day, when hematite first showed substantial nucleation. We hypothesize that during these initial days the Fe(II) uptake rate was controlled by diffusion into ferrihydrite aggregates. Zn concentrations also decreased during this time. While this would appear contradictory with the concept of its rapid release driven be competitive effects, it is possible that as Fe(II) continued to react it underwent electron transfer, with electrons migrating into the bulk mineral structure (Williams and Scherer, 2004; Handler et al., 2009; Boland et al., 2013). This may have reverted the surface of ferrihydrite particles to being dominated by Fe(III), making re-adsorption of Zn more favorable. The slight rebound in dissolved Zn and Fe(II) concentrations after the third day may then relate to the increasing presence of coarser, crystalline iron oxides, which provide less specific surface area and thus a lower capacity to adsorb these species. EXAFS spectroscopy showed that a substantial portion of the Zn initially in ferrihydrite partitions into new mineral phases. This incorporation may thus mute the impact of grain size coarsening on Zn adsorption. A portion of the increase in Zn concentration may also be attributable to Fe(II)-promoted recrystallization of hematite and lepidocrocite (Frierdich et al., 2011; Frierdich and Catalano, 2012; Latta et al., 2012). This has been demonstrated to release structural Zn to solution for hematite (Frierdich and Catalano, 2012). While it has not been clearly demonstrated yet for lepidocrocite, it has been shown for goethite and may be a general phenomenon for crystalline iron oxides (Frierdich and Catalano, 2012; Frierdich et al., 2012).

In the high Fe(II) (1.0 mM) ferrihydrite transformation experiment, dissolved Zn and Fe concentrations behave similarly to what is observed in low Fe(II) experiment. The rapid initial release of Zn plus the rapid decline of both concentrations can again be attributed for the adsorption-desorption processes discussed above. Notably, Zn and Fe concentrations do not rebound at the later stages of reaction, unlike the experiment at lower Fe(II) concentration. A substantial decline in dissolved Fe concentration between day 1 and 3 corresponds to a large increase in magnetite content. Adsorption may thus have been responsible for the initial decline in dissolved Fe concentration to ~0.6 mM, with the larger drop to ~10 μM caused by net Fe(II) consumption during magnetite formation. The near-complete sequestration of Zn in the solid-phase is also likely associated with Zn uptake into the magnetite structure, as indicated by EXAFS spectroscopy. For both systems studied, Zn fate is controlled by both adsorption and incorporation into the secondary iron oxide products.

4.4 Geological and Environmental Implications

4.4.1. Promotion of Low-Temperature Hematite Formation

This study reports rapid formation of hematite from ferrihydrite at 22°C. The presence of Zn clearly accelerates hematite formation, a product not previously observed during Fe(II)-catalyzed ferrihydrite transformation at ambient temperatures (Hansel et al., 2003; Hansel et al., 2005; Pedersen et al., 2005; Yee et al., 2006). The role of Zn itself in forming hematite in natural systems may be limited because it is unlikely that ferrihydrite in the environment will contain Zn at the level (~2 mol.%) explored in the present study, except perhaps near weathering zinc sulfide ore deposits. However, a wide array of substituting elements are commonly associated with iron oxides in nature (Schwertmann and Cornell, 2000; Cornell and Schwertmann, 2003). The present results suggest a general mechanism where substituting elements in ferrihydrite enhance the conversion to hematite, helping to nucleate this phase at temperatures lower than is typically observed in laboratory studies. While further study is warranted, impurities may play key roles in promoting low-temperature hematite formation in the environment.

4.4.2. Potential Impact on Metal Stable Isotope Records

The near-quantitative retention of Zn during Fe(II)-promoted phase transformations, both to ferric oxyhydroxides and to magnetite, suggests that such transformations do not perturb solid-phase trace metal stable isotope compositions. Solid-aqueous fractionation factors between Zn adsorbed to iron oxide minerals and dissolved Zn are generally <0.5‰ in magnitude (Pokrovsky et al., 2005; Balistrieri et al., 2008; Juillot et al., 2008). We are unaware of studies of isotopic fractionation involving Zn incorporated into iron oxides, but adsorption-desorption would be a critical intermediate step that may dictate fractionation. With >97% retention in the solid phase, such partitioning could alter the Zn stable isotope composition of the solid phases by <0.015‰, much less than the typical analytical precision Zn stable isotope measurements (0.04 to 0.1‰) (Balistrieri et al., 2008; Chen et al., 2009; Moynier et al., 2017). This demonstrates that the transformation processes observed in the present study will not measurably alter solid-phase Zn stable isotope compositions from that of primary ferrihydrite precipitates, such as during diagenesis. Conditions that lead to lower Zn retention, such as transformations under more acidic pH, may potentially perturb such values.

4.4.3. Implications for Bioessential Trace Metal Availability

Elements such as cobalt, nickel, copper, and zinc serve as key reaction centers in metalloenzymes (Gärtner et al., 1993; Ermler et al., 1997; Thauer, 1998; Brown et al., 2000; Parks et al., 2013; Zheng et al., 2016) and low availability of these metals may inhibit microbial processes in environment (Schönheit et al., 1979; Granger and Ward, 2003; Ekstrom and Morel, 2008; Glass and Orphan, 2012; Lu et al., 2018). Previous study has suggested that metal solubility can be reduced through coprecipitation with or removal by iron oxides formed during ferrihydrite transformation (Martínez and McBride, 1998). In the current work, the retention of a high portion of Zn in phase transformation products suggests that trace metal micronutrients are not mobilized by formation of more crystalline iron oxides. The observed Zn retention indicates that the availability of this metal is not enhanced during Fe(II)-promoted ferrihydrite transformations except during the first hour of reaction. However, subsequent Zn release during Fe(II)-promoted recrystallization of the more crystalline transformation products (Frierdich et al., 2011; Frierdich and Catalano, 2012) may later enhance metal availability. It is unclear whether similar behavior will be displayed by other bioessential metals, such as Co and Ni, as their solid-water partitioning may be distinct from Zn because of differences in ionic radii and chemical properties.

5. CONCLUSION

The trace metal Zn alters the Fe(II)-induced transformation pathways of ferrihydrite and partially incorporates into the resulting crystalline iron oxides. This study is the first to report that

Zn promotes the formation of hematite at 22°C, which occurs as the dominant reaction product for systems containing 0.2 mM dissolved Fe(II). This suggests that impurity ions may be critical to the formation of hematite in low-temperature environments. In addition, Zn inhibits both goethite formation and the overall transformation of ferrihydrite to more crystalline phases. A small fraction of the ferrihydrite-bound Zn is released to solution during reaction but is rapidly taken back up into the solid phase, partially incorporating into hematite and magnetite. Near-quantitative retention of Zn demonstrates that ferrihydrite phase transformations at pH 7 from interactions with dissolved Fe(II) will preserve the Zn isotopic composition. The Zn to Fe ratio will also be unperturbed except when magnetite or other mixed-valent phases form through net Fe(II) uptake; the additional Fe would dilute the Zn content. Such transformations may thus preserve chemical or isotopic signatures associated with Zn in modern soils or aquatic systems as well as in the sedimentary record. Finally, ferrihydrite phase transformations will not substantially limit trace metal contaminant sequestration or micronutrient availability despite the formation of more crystalline mineral products if fluid conditions favor solid-phase retention.

ACKNOWLEDGEMENT

The project was supported by the International Center for Energy, Environment and Sustainability at Washington University in Saint Louis. Addition support for J.G.C. and J.Y. was provided by the U.S. National Science Foundation (NSF), Environmental Chemical Sciences program through award no. CHE-1709484 and the U.S. Department of Energy (DOE), Office of Science, Office of Biological and Environmental Research, Subsurface Biogeochemical Research program through award no. DE-SC0019422. Preparation of the standards for zinc associated with hematite was supported by the U.S. NSF Faculty Early Career Development Program through award no. EAR-1056480. ICP-MS analyses were performed in the Isotope Cosmochemistry laboratory at the Department of Earth and Planetary Sciences at Washington University. We thank Prof. Kun Wang and Dr. Heng Chen for their help with ICP-MS measurements. BET measurements were conducted at the Nano Research and Environmental Laboratory at Washington University. XAFS data were collected at beamline 12-BM-B at the Advanced Photon Source, a U.S. DOE Office of Science User Facility operated for the DOE Office of Science by Argonne National Laboratory under Contract No. DE-AC02-06CH11357. We thank Dr. Benjamin Reinhart for assistance with XAFS data collection.

APPENDIX A. SUPPLEMENTARY MATERIAL

A supplementary material document associated with this manuscript contains a description of the semi-quantitative determination of ferrihydrite abundance via Rietveld refinement, a description of the EXAFS fitting results for Zn incorporated in and adsorbed on hematite, figures of the Rietveld refinement fitting results, plots of the pH drift over time during the aging experiments, Zn K-edge XANES spectra of Zn-ferrihydrite, its reaction products, and associated standards, and a table of the Rietveld refinement results.

REFERENCES

Ainsworth C. C., Gassman P. L., Pilon J. L. and Van Der Sluys W. G. (1994) Cobalt, cadmium, and lead sorption to hydrous iron oxide: Residence time effect. *Soil Sci. Soc. Am. J.* **58**, 1615–1623.

Ankudinov A. and Ravel B. (1998) Real-space multiple-scattering calculation and interpretation of x-ray-absorption near-edge structure. *Phys. Rev. B - Condens. Matter Mater. Phys.* **58**, 7565–7576.

Balistrieri L. S., Borrok D. M., Wanty R. B. and Ridley W. I. (2008) Fractionation of Cu and Zn isotopes during adsorption onto amorphous Fe(III) oxyhydroxide: Experimental mixing of acid rock drainage and ambient river water. *Geochim. Cosmochim. Acta* **72**, 311–328.

Bekker A., Slack J. F., Planavsky N., Krapež B., Hofmann A., Konhauser K. O. and Rouxel O. J.

(2010) Iron formation: The sedimentary product of a complex interplay among mantle, tectonic, oceanic, and biospheric processes. *Econ. Geol.* **105**, 467–508.

Bergmann J., Friedel P. and Kleeberg R. (1998) BGMN—a new fundamental parameters based Rietveld program for laboratory X-ray sources, its use in quantitative analysis and structure investigations. *CPD Newsl.* **20**, 5–8.

Boland D. D., Collins R. N., Glover C. J. and David Waite T. (2013) An in situ quick-EXAFS and redox potential study of the Fe(II)-catalysed transformation of ferrihydrite. *Colloids Surfaces A Physicochem. Eng. Asp.* **435**, 2–8.

Boland D. D., Collins R. N., Miller C. J., Glover C. J. and Waite T. D. (2014) Effect of solution and solid-phase conditions on the Fe(II)-accelerated transformation of ferrihydrite to lepidocrocite and goethite. *Environ. Sci. Technol.* **48**, 5477–5485.

Brown G. E. and Parks G. A. (2001) Sorption of trace elements on mineral surfaces: Modern perspectives from spectroscopic studies, and comments on sorption in the marine environment. *Int. Geol. Rev.* **43**, 963–1073.

Brown K., Tegoni M., Prudêncio M., Pereira A. S., Besson S., Moura J. J., Moura I. and Cambillau C. (2000) A novel type of catalytic copper cluster in nitrous oxide reductase. *Nat. Struct. Biol.* **7**, 191–195.

Bryan A. L., Dong S., Wilkes E. B. and Wasylenki L. E. (2015) Zinc isotope fractionation during adsorption onto Mn oxyhydroxide at low and high ionic strength. *Geochim. Cosmochim. Acta* **157**, 182–197.

Bylaska E. J., Catalano J. G., Mergelsberg S. T., Saslow S. A., Qafoku O., Prange M. P. and Ilton E. S. (2019) Association of defects and zinc in hematite. *Environ. Sci. Technol.* **53**, 13687–13694.

Chan M. A., Ormö J., Park A. J., Stich M., Souza-Egipsy V. and Komatsu G. (2007) Models of iron oxide concretion formation: Field, numerical, and laboratory comparisons. *Geofluids* **7**, 356–368.

Chen J.-B., Louvat P., Gaillardet J. and Birck J.-L. (2009) Direct separation of Zn from dilute aqueous solutions for isotope composition determination using multi-collector ICP-MS. *Chem. Geol.* **259**, 120–130.

Combes J. M., Manceau A. and Calas G. (1990) Formation of ferric oxides from aqueous solutions: A polyhedral approach by X-ray Absorption Spectroscopy: II. Hematite formation from ferric gels. *Geochim. Cosmochim. Acta* **54**, 1083–1091.

Cornell R. M. (1988) The influence of some divalent cations on the transformation of ferrihydrite to more crystalline products. *Clay Miner.* **23**, 329–332.

Cornell R. M. and Schwertmann U. (2003) *The Iron Oxides*., VCH Publishers, New York.

Dai C., Lin M. and Hu Y. (2017) Heterogeneous Ni- and Cd-bearing ferrihydrite precipitation and recrystallization on quartz under acidic pH condition. *ACS Earth Sp. Chem.* **1**, 621–628.

Das S., Hendry M. J. and Essilfie-Dughan J. (2011) Transformation of two-line ferrihydrite to goethite and hematite as a function of pH and temperature. *Environ. Sci. Technol.* **45**, 268–275.

Doebelin N. and Kleeberg R. (2015) Profex: a graphical user interface for the Rietveld refinement program BGMN. *J. Appl. Crystallogr.* **48**, 1573–1580.

Eickhoff M., Obst M., Schröder C., Hitchcock A. P., Tyliszczak T., Martinez R. E., Robbins L. J., Konhauser K. O. and Kappler A. (2014) Nickel partitioning in biogenic and abiogenic ferrihydrite: The influence of silica and implications for ancient environments. *Geochim. Cosmochim. Acta* **140**, 65–79.

Ekstrom E. B. and Morel F. M. M. (2008) Cobalt limitation of growth and mercury methylation in sulfate-reducing bacteria. *Environ. Sci. Technol.* **42**, 93–99.

Ermler U., Grabarse W., Shima S., Goubeaud M. and Thauer R. K. (1997) Crystal structure of methyl-coenzyme M reductase: The key enzyme of biological methane formation. *Science* **278**, 1457–1462.

Fei Y., Hua J., Liu C., Li F., Zhu Z., Xiao T., Chen M., Gao T., Wei Z. and Hao L. (2018) Aqueous Fe(II)-induced phase transformation of ferrihydrite coupled adsorption/immobilization of rare earth elements. *Minerals* **8**, 357.

Fischer W. R. and Schwertmann U. (1975) The formation of hematite from amorphous iron(III)hydroxide. *Clays Clay Miner.* **23**, 33–37.

Fleet M. E. (1981) The structure of magnetite. *Acta Crystallogr. Sect. B Struct. Crystallogr. Cryst. Chem.* **37**, 917–920.

Ford R. G., Bertsch P. M. and Farley K. J. (1997) Changes in transition and heavy metal partitioning during hydrous iron oxide aging. *Environ. Sci. Technol.* **31**, 2028–2033.

Ford R. G., Kemner K. M. and Bertsch P. M. (1999) Influence of sorbate-sorbent interactions on the crystallization kinetics of nickel- and lead-ferrihydrite coprecipitates. *Geochim. Cosmochim. Acta* **63**, 39–48.

Frierdich A. J. and Catalano J. G. (2012) Controls on Fe(II)-activated trace element release from goethite and hematite. *Environ. Sci. Technol.* **46**, 1519–1526.

Frierdich A. J., Luo Y. and Catalano J. G. (2011) Trace element cycling through iron oxide minerals during redox-driven dynamic recrystallization. *Geology* **39**, 1083–1086.

Frierdich A. J., Scherer M. M., Bachman J. E., Engelhard M. H., Rapponotti B. W. and Catalano J. G. (2012) Inhibition of trace element release during Fe(II)-activated recrystallization of Al-, Cr-, and Sn-substituted goethite and hematite. *Environ. Sci. Technol.* **46**, 10031–10039.

Garçon M., Sauzéat L., Carlson R. W., Shirey S. B., Simon M., Balter V. and Boyet M. (2017) Nitrile, latex, neoprene and vinyl gloves: A primary source of contamination for trace element and Zn isotopic analyses in geological and biological samples. *Geostand. Geoanalytical Res.* **41**, 367–380.

Gärtner P., Ecker A., Fischer R., Linder D., Fuchs G. and Thauer R. K. (1993) Purification and properties of N5-methyltetrahydromethanopterin: coenzyme M methyltransferase from Methanobacterium thermoautotrophicum. *Eur. J. Biochem.* **213**, 537–545.

Glass J. B. and Orphan V. J. (2012) Trace metal requirements for microbial enzymes involved in the production and consumption of methane and nitrous oxide. *Front. Microbiol.* **3**, 1–20.

Granger J. and Ward B. B. (2003) Accumulation of nitrogen oxides in copper-limited cultures of denitrifying bacteria. *Limnol. Oceanogr.* **48**, 313–318.

Gustafsson J. P., Tiberg C., Edkymish A. and Kleja D. B. (2011) Modelling lead(II) sorption to ferrihydrite and soil organic matter. *Environ. Chem.* **8**, 485–492.

Ha J., Trainor T. P., Farges F. and Brown G. E. (2009) Interaction of aqueous Zn(II) with hematite nanoparticles and microparticles. Part 1. EXAFS study of Zn(II) adsorption and precipitation. *Langmuir* **25**, 5574–5585.

Handler R. M., Beard B. L., Johnson C. M. and Scherer M. M. (2009) Atom exchange between aqueous Fe (II) and goethite : An Fe isotope tracer study. **43**, 1102–1107.

Hansel C. M., Benner S. G. and Fendorf S. (2005) Competing Fe(II)-induced mineralization pathways of ferrihydrite. *Environ. Sci. Technol.* **39**, 7147–7153.

Hansel C. M., Benner S. G., Neiss J., Dohnalkova A., Kukkadapu R. K. and Fendorf S. (2003) Secondary mineralization pathways induced by dissimilatory iron reduction of ferrihydrite under advective flow. *Geochim. Cosmochim. Acta* **67**, 2977–2992.

Hansel C. M., Learman D. R., Lentini C. J. and Ekstrom E. B. (2011) Effect of adsorbed and substituted Al on Fe(II)-induced mineralization pathways of ferrihydrite. *Geochim. Cosmochim. Acta* **75**, 4653–4666.

Hiemstra T. (2015) Formation, stability, and solubility of metal oxide nanoparticles: Surface entropy, enthalpy, and free energy of ferrihydrite. *Geochim. Cosmochim. Acta* **158**, 179–198.

Hiemstra T. (2013) Surface and mineral structure of ferrihydrite. *Geochim. Cosmochim. Acta* **105**, 316–325.

Hiemstra T., Mendez J. C. and Li J. (2019) Evolution of the reactive surface area of ferrihydrite: Time, pH, and temperature dependency of growth by Ostwald ripening. *Environ. Sci. Nano* **6**, 820–833.

Jambor J. L. and Dutrizac J. E. (1998) Occurrence and constitution of natural and synthetic ferrihydrite, a widespread iron oxyhydroxide. *Chem. Rev.* **98**, 2549–2585.

Jiang Z., Liu Q., Roberts A. P., Barrón V., Torrent J. and Zhang Q. (2018) A new model for transformation of ferrihydrite to hematite in soils and sediments. *Geology* **46**, 987–990.

Johnston J. H. and Lewis D. G. (1983) A detailed study of the transformation of ferrihydrite to hematite in an aqueous medium at 92°C. *Geochim. Cosmochim. Acta* **47**, 1823–1831.

Jones A. M., Collins R. N., Rose J. and Waite T. D. (2009) The effect of silica and natural organic matter on the Fe(II)-catalysed transformation and reactivity of Fe(III) minerals. *Geochim. Cosmochim. Acta* **73**, 4409–4422.

Jones A. M., Collins R. N. and Waite T. D. (2017) Redox characterization of the Fe(II)-catalyzed transformation of ferrihydrite to goethite. *Geochim. Cosmochim. Acta* **218**, 257–272.

Juillot F., Maréchal C., Ponthieu M., Cacaly S., Morin G., Benedetti M., Hazemann J. L., Proux O. and Guyot F. (2008) Zn isotopic fractionation caused by sorption on goethite and 2-Lines ferrihydrite. *Geochim. Cosmochim. Acta* **72**, 4886–4900.

Kämpf N. and Schwertmann U. (1983) Goethite and hematite in a climosequence in southern Brazil and their application in classification of kaolinitic soils. *Geoderma* **29**, 27–39.

Kay A. R. (2004) Detecting and minimizing zinc contamination in physiological solutions. *BMC Physiol.* **4**, 1–9.

Kelly S. D., Hesterberg D. and Ravel B. (2008) Analysis of soils and minerals Using X-ray absorption spectroscopy. In *Methods of Soil Analysis* Soil Science Society of America, Madison. pp. 387–463.

Latta D. E., Gorski C. A. and Scherer M. M. (2012) Influence of Fe 2+ -catalysed iron oxide recrystallization on metal cycling. *Biochem. Soc. Trans.* **40**, 1191–1197.

Lee K., Kostka J. E. and Stucki J. W. (2006) Comparisons of structural Fe reduction in smectites by bacteria and dithionite: An infrared spectroscopic study. *Clays Clay Miner.* **54**, 195–208.

Liu C., Zhu Z., Li F., Liu T., Liao C., Lee J. J., Shih K., Tao L. and Wu Y. (2016) Fe(II)-induced phase transformation of ferrihydrite: The inhibition effects and stabilization of divalent metal cations. *Chem. Geol.* **444**, 110–119.

Liu H., Guo H., Li P. and Wei Y. (2008) The transformation of ferrihydrite in the presence of trace Fe(II): The effect of the anionic media. *J. Solid State Chem.* **181**, 2666–2671.

Liu H., Li P., Zhu M., Wei Y. and Sun Y. (2007) Fe(II)-induced transformation from ferrihydrite to lepidocrocite and goethite. *J. Solid State Chem.* **180**, 2121–2128.

Liu H., Wei Y. and Sun Y. (2005) The Formation of hematite from ferrihydrite using Fe(II) as a catalyst. *J. Mol. Catal. A Chem.* **226**, 135–140.

Lu X., Johs A., Zhao L., Wang L., Pierce E. M. and Gu B. (2018) Nanomolar copper enhances mercury methylation by desulfovibrio desulfuricans ND132. *Environ. Sci. Technol. Lett.* **5**, 372–376.

Maillot F., Morin G., Wang Y., Bonnin D., Ildefonse P., Chaneac C. and Calas G. (2011) New insight into the structure of nanocrystalline ferrihydrite: EXAFS evidence for tetrahedrally coordinated iron(III). *Geochim. Cosmochim. Acta* **75**, 2708–2720.

Manceau A., Lanson M. and Geoffroy N. (2007) Natural speciation of Ni, Zn, Ba, and As in ferromanganese coatings on quartz using X-ray fluorescence, absorption, and diffraction. *Geochim. Cosmochim. Acta* **71**, 95–128.

Martínez C. E. and McBride M. B. (1998) Coprecipitates of Cd, Cu, Pb and Zn in iron oxides: Solid phase transformation and metal solubility after aging and thermal treatment. *Clays Clay Miner.* **46**, 537–545.

Masue-Slowey Y., Loeppert R. H. and Fendorf S. (2011) Alteration of ferrihydrite reductive dissolution and transformation by adsorbed As and structural Al: Implications for As retention. *Geochim. Cosmochim. Acta* **75**, 870–886.

Michel F. M., Barrón V., Torrent J., Morales M. P., Serna C. J., Boily J. F., Liu Q., Ambrosini A., Cismasu A. C. and Brown G. E. (2010) Ordered ferrimagnetic form of ferrihydrite reveals links among structure, composition, and magnetism. *Proc. Natl. Acad. Sci. U. S. A.* **107**, 2787–2792.

Michel F. M., Ehm L., Antao S. M., Lee P. L., Chupas P. J., Liu G., Strongin D. R., Schoonen M. A. A., Phillips B. L. and Parise J. B. (2007) The structure of ferrihydrite, a nanocrystalline material. *Science* **316**, 1726–1729.

Moynier F., Vance D., Fujii T. and Savage P. (2017) The isotope geochemistry of zinc and copper. *Rev. Mineral. Geochemistry* **82**, 543–600.

Nagano T., Nakashima S., Nakayama S. and Senoo M. (1994) The use of color to quantify the effects of pH and temperature on the crystallization kinetics of goethite under highly alkaline conditions. *Clays Clay Miner.* **42**, 226–234.

Navrotsky A., Mazeina L. and Majzlan J. (2008) Size-driven structural and thermodynamic complexity in iron oxides. *Science* **319**, 1635–1638.

Newville M. (2001) IFEFFIT: Interactive XAFS analysis and FEFF fitting. *J. Synchrotron Radiat.* **8**, 322–324.

Nørnberg P., Vendelboe A. L., Gunnlaugsson H. P., Merrison J. P., Finster K. and Jensen S. K. (2009) Comparison of the mineralogical effects of an experimental forest fire on a goethite/ferrihydrite soil with a topsoil that contains hematite, maghemite and goethite. *Clay Miner.* **44**, 239–247.

Parks J. M., Johs A., Podar M., Bridou R., Hurt R. A., Smith S. D., Tomanicek S. J., Qian Y., Brown S. D., Brandt C. C., Palumbo A. V., Smith J. C., Wall J. D., Elias D. A. and Liang L. (2013) The genetic basis for bacterial mercury methylation. *Science* **339**, 1332–1335.

Pavese A., Levy D. and Hoser A. (2000) Cation distribution in synthetic zinc ferrite (Zn0.97Fe2.02O4) from in situ high-temperature neutron powder diffraction. *Am. Mineral.* **85**, 1497–1502.

Pedersen H. D., Postma D., Jakobsen R. and Larsen O. (2005) Fast transformation of iron oxyhydroxides by the catalytic action of aqueous Fe(II). *Geochim. Cosmochim. Acta* **69**, 3967–3977.

Pokrovsky O. S., Viers J. and Freydier R. (2005) Zinc stable isotope fractionation during its adsorption on oxides and hydroxides. *J. Colloid Interface Sci.* **291**, 192–200.

Ravel B. and Newville M. (2005) ATHENA, ARTEMIS, HEPHAESTUS: Data analysis for X-ray absorption spectroscopy using IFEFFIT. *J. Synchrotron Radiat.* **12**, 537–541.

Sakakibara M., Tanaka M., Takahashi Y. and Murakami T. (2019) Redistribution of Zn during transformation of ferrihydrite: Effects of initial Zn concentration. *Chem. Geol.* **522**, 121–134.

Scheinost A. C., Abend S., Pandya K. I. and Sparks D. L. (2001) Kinetic controls on Cu and Pb sorption by ferrihydrite. *Environ. Sci. Technol.* **35**, 1090–1096.

Schönheit P., Moll J. and Thauer R. K. (1979) Nickel, cobalt, and molybdenum requirement for growth of Methanobacterium thermoautotrophicum. *Arch. Microbiol.* **123**, 105–107.

Schultz M. F., Benjamin M. M. and Ferguson J. F. (1987) Adsorption and desorption of metals on ferrihydrite: Reversibility of the reaction and sorption properties of the regenerated solid. *Environ. Sci. Technol.* **21**, 863–869.

Schwertmann U. and Cornell R. M. (2000) *Iron Oxides in the Laboratory: Preparation and Synthesis*., VCH Publishers, New York.

Schwertmann U., Friedl J. and Stanjek H. (1999) From Fe(III) ions to ferrihydrite and then to hematite. *J. Colloid Interface Sci.* **223**, 215–223.

Schwertmann U., Friedl J., Stanjek H. and Schulze D. G. (2000a) The effect of Al on Fe oxides. XIX. Formation of Al-substituted hematite from ferrihydrite at 25°C and pH 4 to 7. *Clays Clay Miner.* **48**, 159–172.

Schwertmann U., Friedl J., Stanjek H. and Schulze D. G. (2000b) The effect of clay minerals on the formation of goethite and hematite from ferrihydrite after 16 years' ageing at 25°C and pH 4-7. *Clay Miner.* **35**, 613–623.

Schwertmann U. and Murad E. (1983) Effect of pH on the formation of goethite and hematite from ferrihydrite. *Clays Clay Miner.* **31**, 277–284.

Schwertmann U., Stanjek H. and Becher H.-H. (2004) Long-term in vitro transformation of 2-line ferrihydrite to goethite/hematite at 4, 10, 15 and 25°C . *Clay Miner.* **39**, 433–438.

Schwertmann U. and Taylor R. M. (1972) The transformation of lepidocrocite to goethite. *Clays Clay Miner.* **20**, 151–158.

Sheng A., Li X., Arai Y., Ding Y., Rosso K. M. and Liu J. (2020a) Citrate controls Fe(II)-catalyzed transformation of ferrihydrite by complexation of the labile Fe(III) intermediate. *Environ. Sci. Technol.* **54**, 7309–7319.

Sheng A., Liu J., Li X., Qafoku O., Collins R. N., Jones A. M., Pearce C. I., Wang C., Ni J., Lu A. and Rosso K. M. (2020b) Labile Fe(III) from sorbed Fe(II) oxidation is the key intermediate in Fe(II)-catalyzed ferrihydrite transformation. *Geochim. Cosmochim. Acta* **272**, 105–120.

Soltis J. A., Feinberg J. M., Gilbert B. and Penn R. L. (2016) Phase transformation and particle-mediated growth in the formation of hematite from 2-Line ferrihydrite. *Cryst. Growth Des.* **16**, 922–932.

Thauer R. K. (1998) Biochemistry of methanogenesis: a tribute to Marjory Stephenson:1998 Marjory Stephenson Prize Lecture. *Microbiology* **144**, 2377–2406.

Thomasarrigo L. K., Byrne J. M., Kappler A. and Kretzschmar R. (2018) Impact of organic matter on iron(II)-catalyzed mineral transformations in ferrihydrite-organic matter coprecipitates. *Environ. Sci. Technol.* **52**, 12316–12326.

Thomasarrigo L. K., Kaegi R. and Kretzschmar R. (2019) Ferrihydrite growth and transformation in the presence of ferrous iron and model organic ligands. *Environ. Sci. Technol.* **53**, 13636–13647.

Tian L., Shi Z., Lu Y., Dohnalkova A. C., Lin Z. and Dang Z. (2017) Kinetics of cation and oxyanion adsorption and desorption on ferrihydrite: Roles of ferrihydrite binding sites and a unified model. *Environ. Sci. Technol.* **51**, 10605–10614.

Tomaszewski E. J., Cronk S. S., Gorski C. A. and Ginder-Vogel M. (2016) The role of dissolved Fe(II) concentration in the mineralogical evolution of Fe (hydr)oxides during redox cycling. *Chem. Geol.* **438**, 163–170.

Torrent J., Guzman R. and Parra M. A. (1982) Influence of relative humidity on the crystallization of Fe(III) oxides from ferrihydrite. *Clays Clay Miner.* **30**, 337–340.

Tronc E., Belleville P., Jolivet J. P. and Livage J. (1992) Transformation of ferric hydroxide into spinel by Fe(II) adsorption. *Langmuir* **8**, 313–319.

Verwey E. J. W. and Heilmann E. L. (1947) Physical properties and cation arrangement of oxides with spinel structures I. Cation arrangement in spinels. *J. Chem. Phys.* **15**, 174–180.

Wang X., Zhu M., Lan S., Ginder-Vogel M., Liu F. and Feng X. (2015) Formation and secondary mineralization of ferrihydrite in the presence of silicate and Mn(II). *Chem. Geol.* **415**, 37–46.

Waychunas G. A., Fuller C. C. and Davis J. A. (2002) Surface complexation and precipitate geometery for aqueous Zn(II) sorption on ferrihydrite I: X-ray absorption extended fine structure spectroscopy analysis. *Geochim. Cosmochim. Acta* **66**, 1119–1137.

Webb S. M. (2005) SIXpack: A graphical user interface for XAS analysis using IFEFFIT. *Phys. Scr. T* **T115**, 1011–1014.

Williams A. G. B. and Scherer M. M. (2004) Spectroscopic evidence for Fe(II)-Fe(III) electron transfer at the iron oxide-water interface. *Environ. Sci. Technol.* **38**, 4782–4790.

Xiao W., Jones A. M., Collins R. N. and Waite T. D. (2018) Investigating the effect of ascorbate on the Fe(II)-catalyzed transformation of the poorly crystalline iron mineral ferrihydrite. *Biochim. Biophys. Acta - Gen. Subj.* **1862**, 1760–1769.

Yang L., Steefel C. I., Marcus M. A. and Bargar J. R. (2010) Kinetics of Fe(II)-catalyzed transformation of 6-line ferrihydrite under anaerobic flow conditions. *Environ. Sci. Technol.* **44**, 5469–5475.

Yee N., Shaw S., Benning L. G. and Nguyen T. H. (2006) The rate of ferrihydrite transformation to goethite via the Fe(II) pathway. *Am. Mineral.* **91**, 92–96.

Zhang D., Wang S., Wang Y., Gomez M. A., Duan Y. and Jia Y. (2018) The transformation of two-line ferrihydrite into crystalline products: effect of pH and media (sulfate versus nitrate). *ACS Earth Sp. Chem.* **2**, 577–587.

Zheng K., Ngo P. D., Owens V. L., Yang X. P. and Mansoorabadi S. O. (2016) The biosynthetic pathway of coenzyme F430 in methanogenic and methanotrophic archaea. *Science* **354**, 339–342.

Zhou Z., Latta D. E., Noor N., Thompson A., Borch T. and Scherer M. M. (2018) Fe(II)-catalyzed transformation of organic matter-ferrihydrite coprecipitates: A closer look using Fe isotopes. *Environ. Sci. Technol.* **52**, 11142–11150.

Table 1. Results of structural model fitting of Zn K-edge EXAFS spectra.

Sample	**Shell**	**N**[a]	**R (Å)**[b]	**σ^2 (Å^2)**[c]	**ΔE_0 (eV)**[d]	**χ_v^2**[e]
Zn-ferrihydrite	O	4.2(4)[f]	1.97(1)	0.0064(9)	0(1)	18.88
	Fe	6(2)	3.45(1)	0.017(3)		
Zn-hematite	O	3	1.98(1)	0.0052(9)	1(2)	13.32
	O	3	2.20(2)	0.013(3)		
	Fe	3.5(3)	2.98(1)	0.008		
	Fe	1.4(4)	3.33(2)	0.008		
Zn adsorbed to hematite	O	6.2(5)	2.014(6)	0.012(1)	-2(1)	2.15
	Fe	0.2(2)	3.28(6)	0.008		
0.2 mM Fe(II), 2 hr	O	3.9(5)	1.966(8)	0.006(1)	1(1)	14.64
	Fe	6(3)	3.43(2)	0.018(5)		
0.2 mM Fe(II), 12 d	O	3.0(2)	1.98(1)	0.004(1)	1(2)	3.30
	O	1.6(2)	2.14(2)	0.004(1)		
	Fe	0.8(2)	2.98(2)	0.008		
	Fe	0.7(3)	3.39(3)	0.008		
1.0 mM Fe(II), 12 d	O	4(1)	1.97(1)	0.005(2)	1(2)	15.44
	Fe	18(5)	3.50(2)	0.015(3)		

[a] Coordination number. [b] Interatomic distance. [c] Debye-Waller factor. [d] Difference in the threshold Fermi level between data and theory. [e] Reduced chi squared, a goodness-of-fit parameter (Kelly et al., 2008). [f] Values in parentheses are fitting uncertainties in the last digit, reported at the 1σ level. Parameters without uncertainties were held constant during fitting.

Figure Captions

Figure 1. (a) XRD patterns of as-synthesized Zn-free ferrihydrite and Zn-ferrihydrite. (b) Data (dotted) and structural model fit (lines) of Zn K-edge EXAFS spectra (left) and Fourier Transform magnitude (right) of Zn-ferrihydrite.

Figure 2. XRD patterns of the solid phase products of Zn-ferrihydrite reaction with (top) 0.2 mM Fe(II) and (bottom) 1.0 mM Fe(II). Diagnostic peaks are labeled to indicate mineral phases: F=ferrihydrite, L=lepidocrocite, H=hematite, M=magnetite.

Figure 3. Fractional abundances of crystalline minerals (top) and of all minerals present (bottom) determined by Rietveld refinement for reaction of 0.2 mM dissolved Fe(II) with Zn-ferrihydrite (left) or a Zn-free ferrihydrite control (right).

Figure 4. Fractional abundances of crystalline minerals (top) and of all minerals present (bottom) determined by Rietveld refinement for reaction of 1.0 mM dissolved Fe(II) with Zn-ferrihydrite (left) or a Zn-free ferrihydrite control (right).

Figure 5. XRD patterns of (A) initial Zn-ferrihydrite (Zn-fh) and Zn-ferrihydrite aged for 12 days in the absence of Fe(II); (B) initial Zn-free ferrihydrite (fh) and Zn-free ferrihydrite reacted with 0.2 mM Fe(II) or 1.0 mM Fe(II) for 12 days. Diagnostic peaks are labeled to indicate mineral phases: F=ferrihydrite, L=lepidocrocite, H=hematite, G=goethite, M=magnetite.

Figure 6. Dissolved Zn and Fe concentrations change with time during Zn-ferrihydrite transformation induced by 0.2 mM Fe(II) and 1.0 mM Fe(II)

Figure 7. Data (dotted) and structural model fit (lines) of Zn K-edge EXAFS spectra and Fourier Transform magnitude of samples and standards associated with aging of Zn-ferrihydrite with (top) 0.2 mM Fe(II) and (bottom) 1.0 mM Fe(II). Individual spectra are: (a) unreacted Zn-

ferrihydrite; Zn-ferrihydrite reacted with 0.2 mM Fe(II) for (b) 2 hours and (c) 12 days; (d) Zn substituted in hematite; (e) Zn adsorbed to hematite; (f) Zn-ferrihydrite reacted with 1.0 mM Fe(II) for 12 days; (g) franklinite ($ZnFe_2O_4$).

Figure 8. Data (black circles) and linear combination fit (red line) of Zn K-edge EXAFS spectra of Zn-ferrihydrite reacted with 0.2 mM Fe(II) for 2 hours and 12 days and with 1.0 mM Fe(II) for 12 days.

Figures

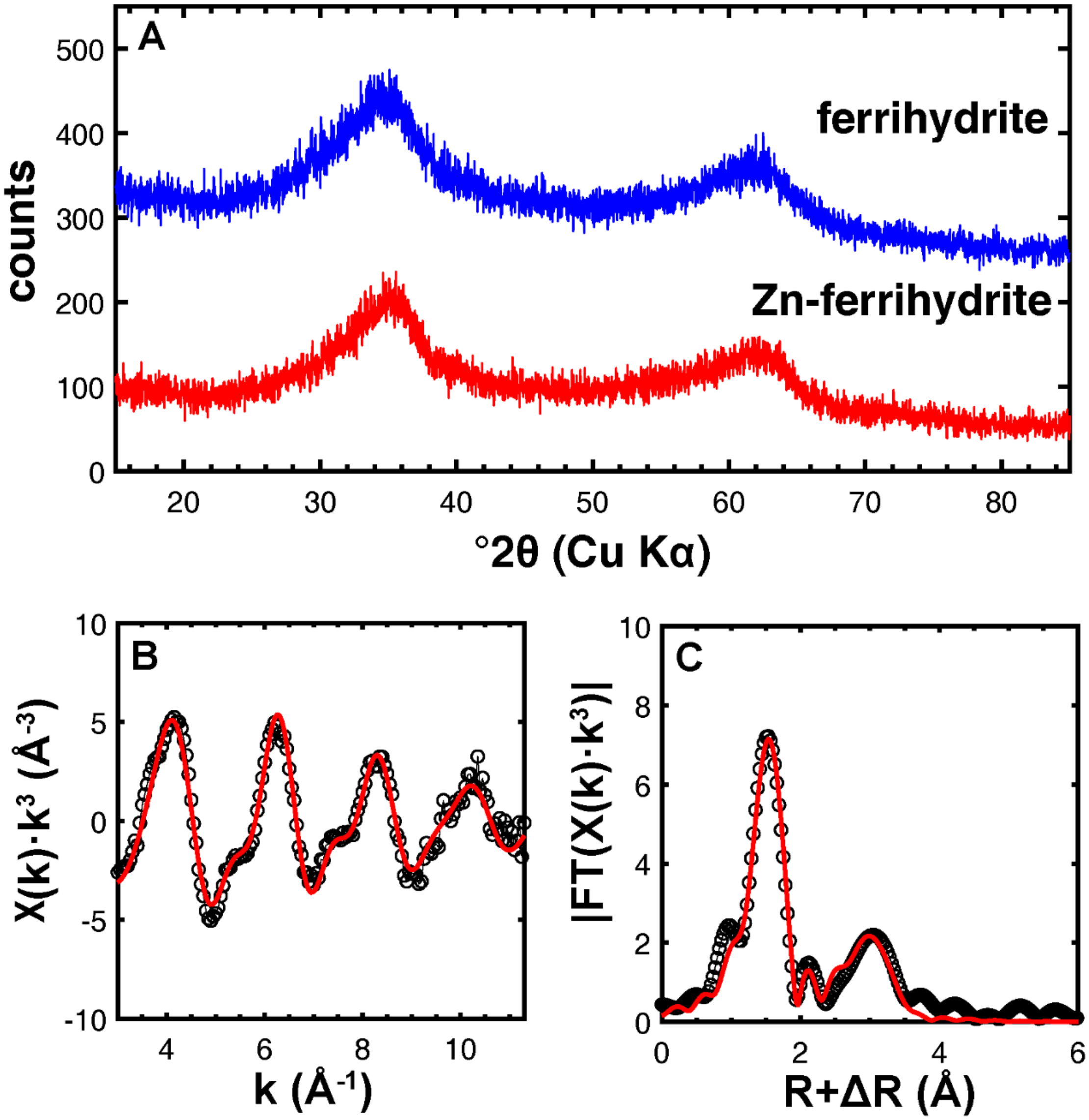

Figure 1. (a) XRD patterns of as-synthesized Zn-free ferrihydrite and Zn-ferrihydrite. (b) Data (dotted) and structural model fit (lines) of Zn K-edge EXAFS spectra (left) and Fourier Transform magnitude (right) of Zn-ferrihydrite.

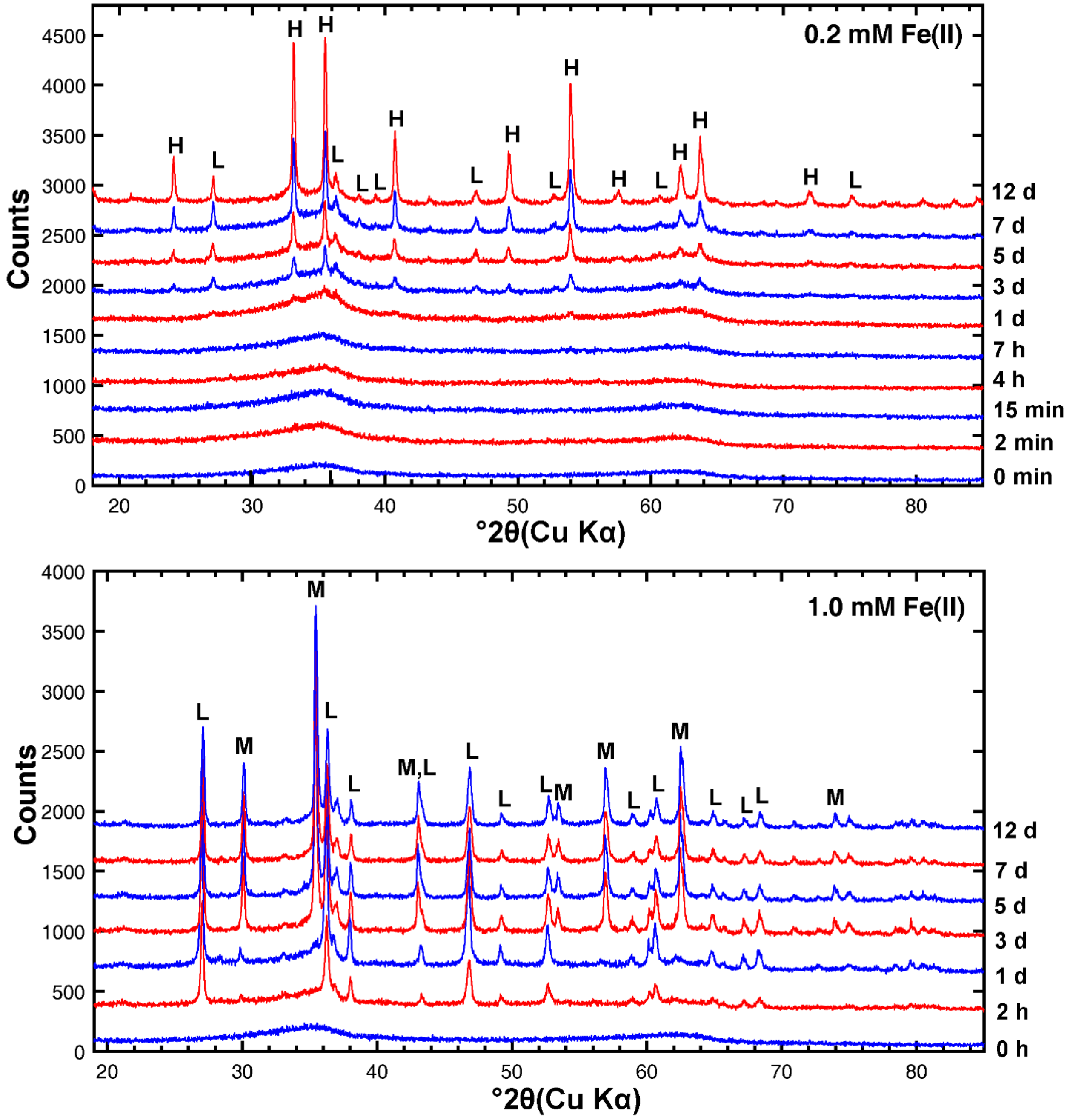

Figure 2. XRD patterns of the solid phase products of Zn-ferrihydrite reaction with (top) 0.2 mM Fe(II) and (bottom) 1.0 mM Fe(II). Diagnostic peaks are labeled to indicate mineral phases: F=ferrihydrite, L=lepidocrocite, H=hematite, M=magnetite.

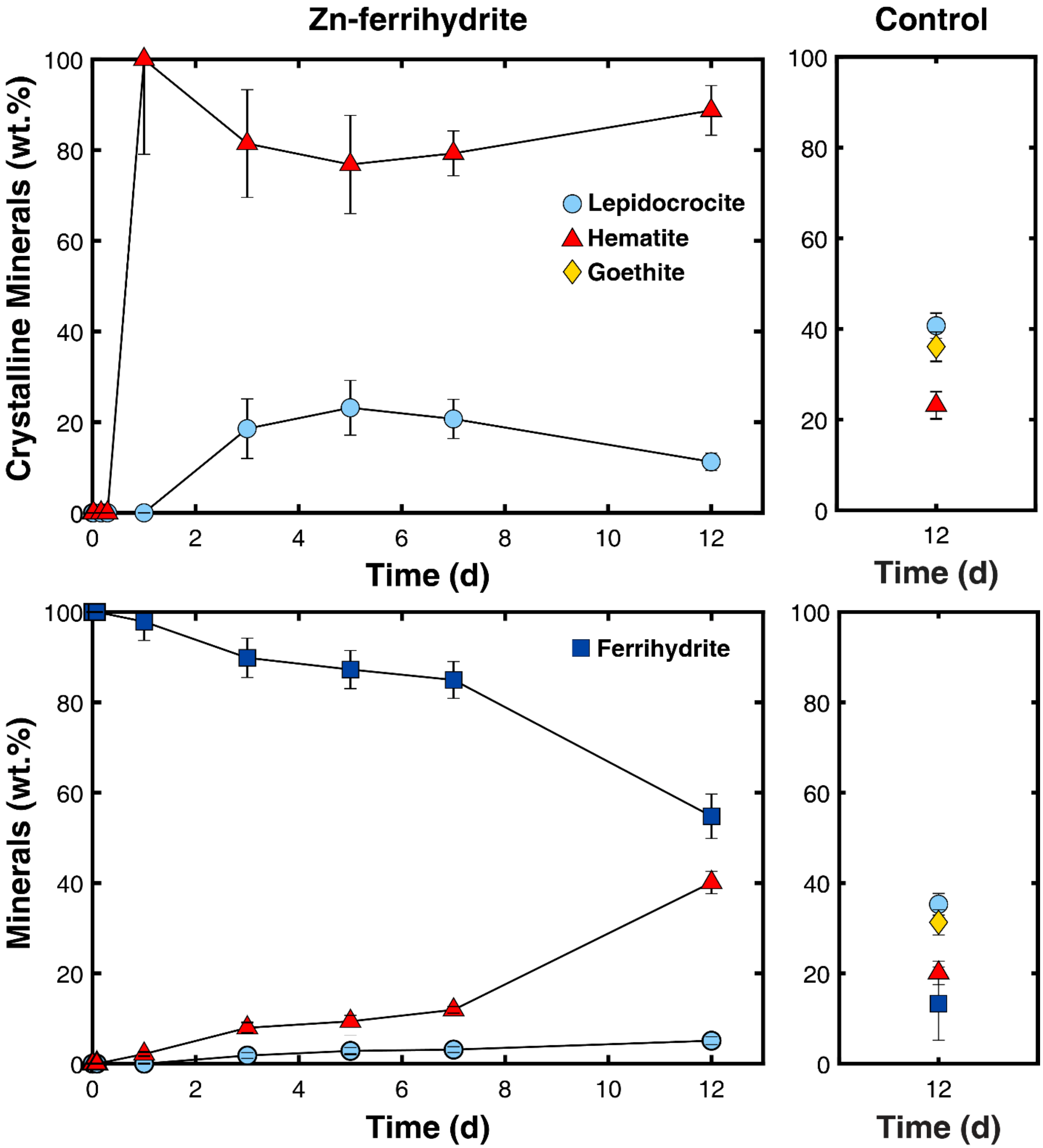

Figure 3. Fractional abundances of crystalline minerals (top) and of all minerals present (bottom) determined by Rietveld refinement for reaction of 0.2 mM dissolved Fe(II) with Zn-ferrihydrite (left) or a Zn-free ferrihydrite control (right).

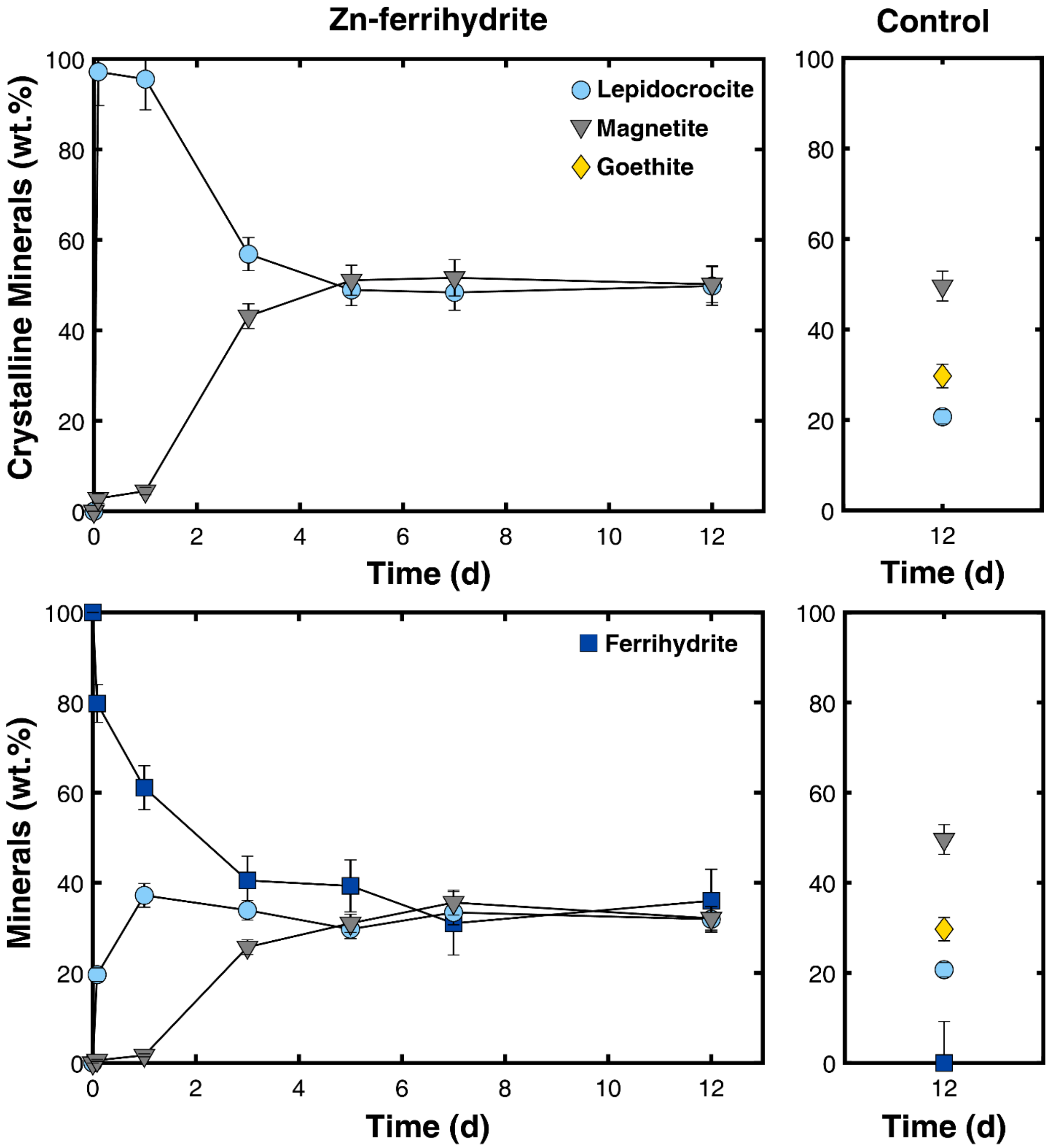

Figure 4. Fractional abundances of crystalline minerals (top) and of all minerals present (bottom) determined by Rietveld refinement for reaction of 1.0 mM dissolved Fe(II) with Zn-ferrihydrite (left) or a Zn-free ferrihydrite control (right).

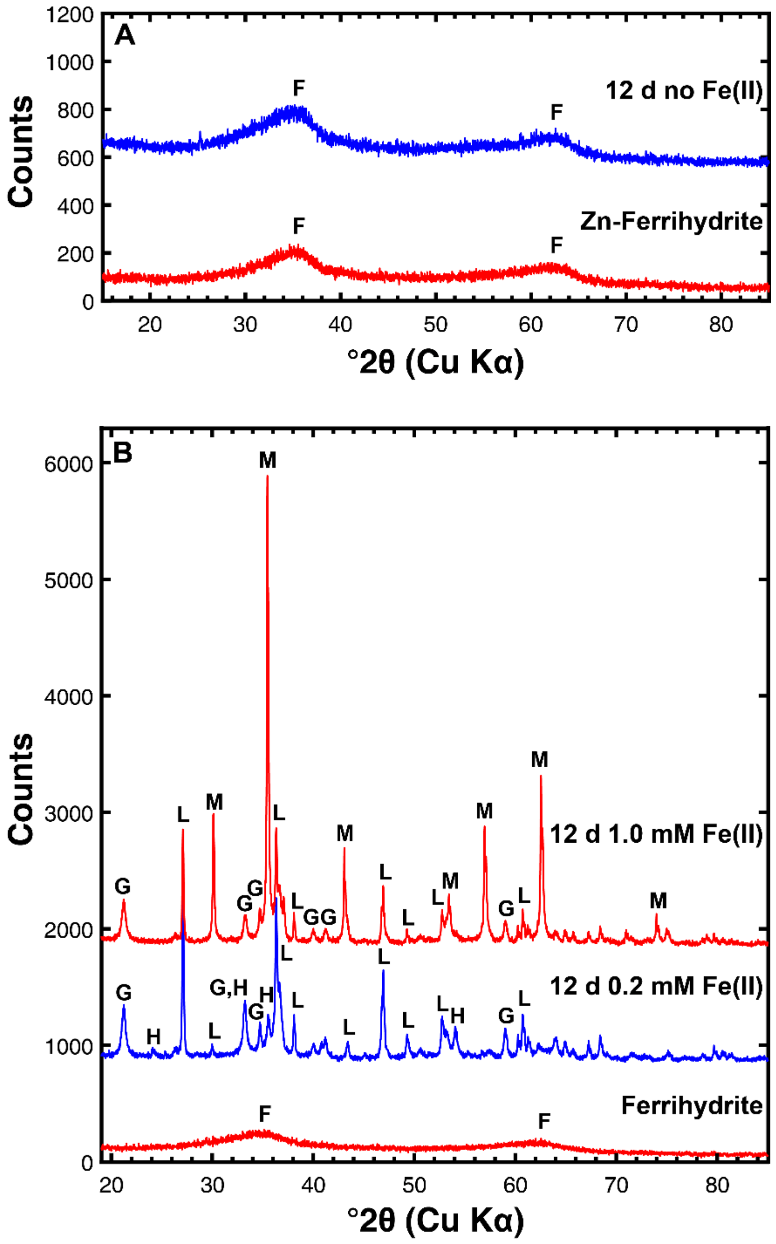

Figure 5. XRD patterns of (A) initial Zn-ferrihydrite (Zn-fh) and Zn-ferrihydrite aged for 12 days in the absence of Fe(II); (B) initial Zn-free ferrihydrite (fh) and Zn-free ferrihydrite reacted with 0.2 mM Fe(II) or 1.0 mM Fe(II) for 12 days. Diagnostic peaks are labeled to indicate mineral phases: F=ferrihydrite, L=lepidocrocite, H=hematite, G=goethite, M=magnetite.

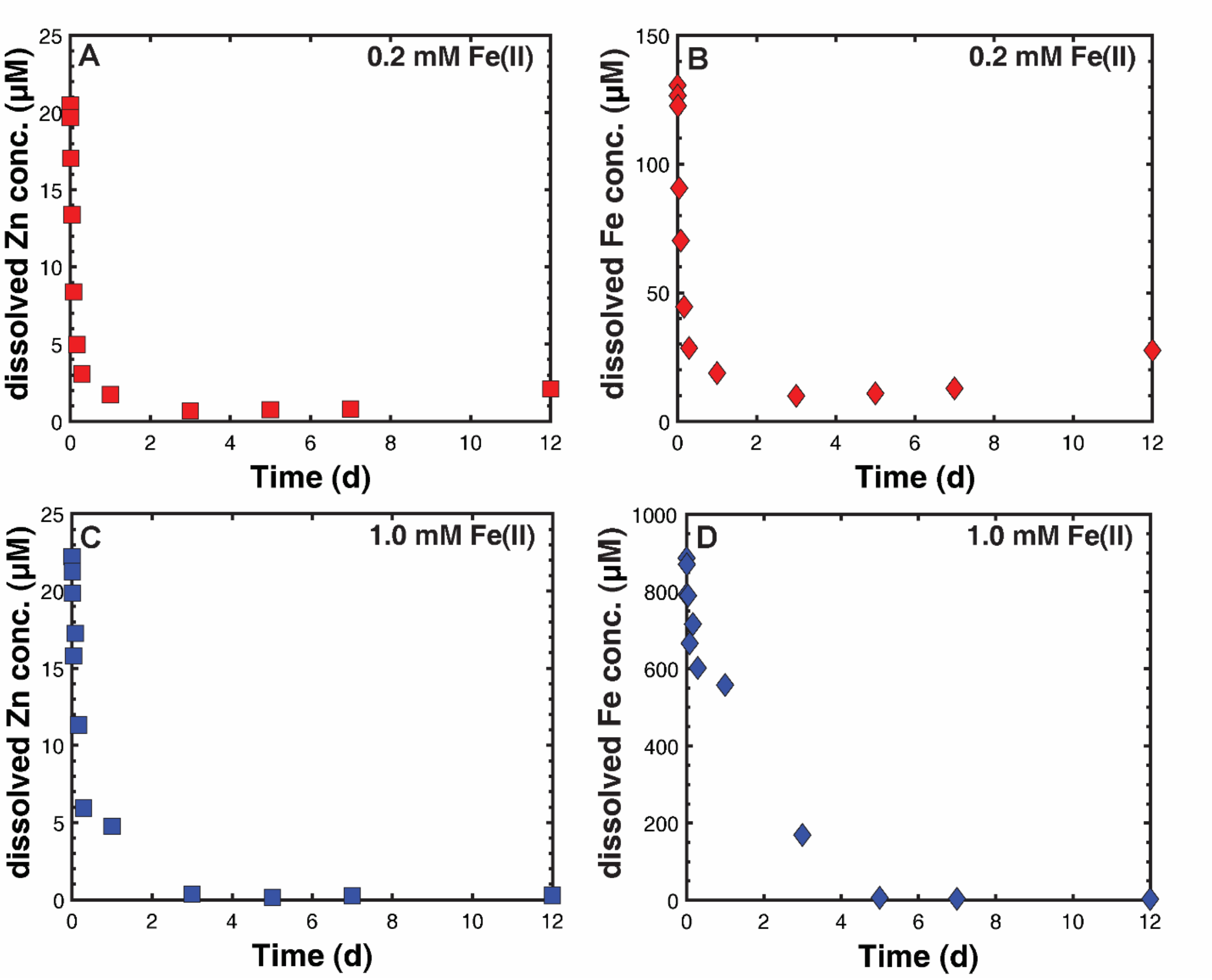

Figure 6. Dissolved Zn and Fe concentrations change with time during Zn-ferrihydrite transformation induced by 0.2 mM Fe(II) and 1.0 mM Fe(II)

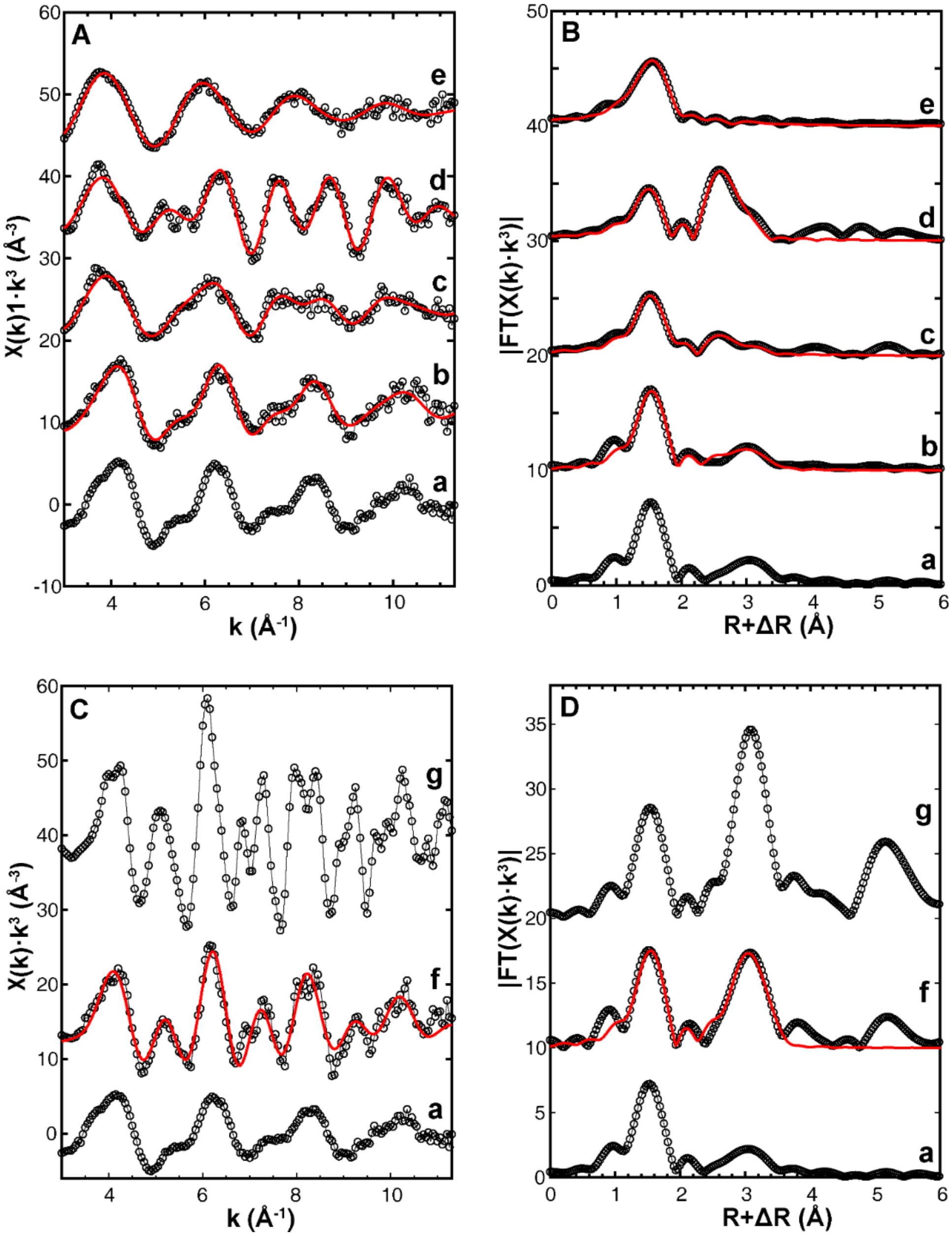

Figure 7. Data (dotted) and structural model fit (lines) of Zn K-edge EXAFS spectra and Fourier Transform magnitude of samples and standards associated with aging of Zn-ferrihydrite with (top) 0.2 mM Fe(II) and (bottom) 1.0 mM Fe(II). Individual spectra are: (a) unreacted Zn-ferrihydrite; Zn-ferrihydrite reacted with 0.2 mM Fe(II) for (b) 2 hours and (c) 12 days; (d) Zn substituted in hematite; (e) Zn adsorbed to hematite; (f) Zn-ferrihydrite reacted with 1.0 mM Fe(II) for 12 days; (g) franklinite ($ZnFe_2O_4$).

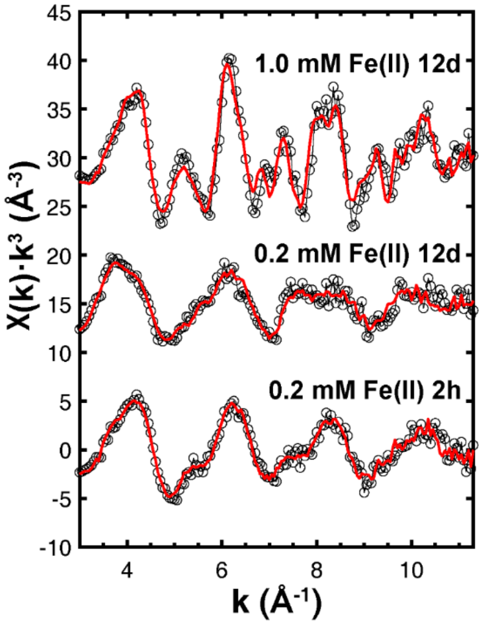

Figure 8. Data (black circles) and linear combination fit (red line) of Zn K-edge EXAFS spectra of Zn-ferrihydrite reacted with 0.2 mM Fe(II) for 2 hours and 12 days and with 1.0 mM Fe(II) for 12 days.

Supplementary Material for:

Impact of Zn Substitution on Fe(II)-induced Ferrihydrite Transformation Pathways

Jinshu Yan[1], Andrew J. Frierdich[2], and Jeffrey G. Catalano[1*]

1. Department of Earth and Planetary Sciences, Washington University in St. Louis, Saint Louis, MO 63130, USA
2. School of Earth, Atmosphere & Environment, Monash University, Clayton, VIC 3800, Australia
*Corresponding author: catalano@wustl.edu

Semi-Quantitative Ferrihydrite Abundance Determined via Rietveld Refinement

The nanocrystalline nature of ferrihydrite precludes accurate simulation of its powder diffraction pattern, including the intensity of features. This prevents the use of Rietveld refinements for quantitative ferrihydrite determination using XRD data. However, full pattern simulation based on a fixed structural model and sample-specific parameters (e.g., peak broadening) that reproduces a measured pattern may provide a means for semi-quantitative analysis in a Rietveld framework under controlled experimental conditions. Full pattern calculations derived from a crystal structure provide scattering intensities determined from atomic scattering factors and thus should respond to abundance changes. However, the broad nature of ferrihydrite scattering features also pose challenges in distinguishing these from background, especially at low abundances.

The semi-quantitative analysis of ferrihydrite via Rietveld refinement was thus first evaluated using mixtures with a zinc oxide standard (U.S. National Bureau of Standards SRM 674). All analysis was conducted in the Profex interface to BGMN. First, the XRD pattern of synthetic Zn-ferrihydrite was simulated (Fig. 1) with the crystal structure of 2 nm ferrihydrite from (Michel et al., 2007). Only the lattice parameters and a peak broadening term were allowed to vary, and the values from this initial analysis were then fixed for all subsequent analyses. Next, a series of mixtures of ferrihydrite and zinc oxide, including both pure endmembers, were analyzed via Rietveld refinement as a two-component mixture. The recovered ferrihydrite abundances (Fig. S1a) varied linearly with true abundance but overestimated the ferrihydrite content as its concentration decreased. A calibration curve between fitted and actual ferrihydrite abundance was generated using linear regression, with the uncertainties on the slope and intercept propagated through calculation of actual ferrihydrite abundance for unknown samples.

The accuracy of this calibration curve was next tested using data collected for synthetic mixtures of ferrihydrite and hematite. The values derived from fitting the XRD patterns of these mixtures via Rietveld refinement and then applying the calibration curve described above generally well-reproduced the true ferrihydrite abundance within ±5 wt.%, and within the one-sigma fitting uncertainty for all but one sample (Fig. S1b,c). Fitting uncertainties are likely underestimated at low ferrihydrite abundances because the calibration curve was generated using unweighted linear regression. While a weighted linear regression to account for the different uncertainties derived from Rietveld refinement of the initial ferrihydrite-zinc oxide data would provide a more accurate estimate of the confidence interval, it is not trivial to then propagate this through the calculation to derive actual ferrihydrite abundances. The ferrihydrite determination should thus be viewed as semi-quantitative, primarily because of underestimated uncertainties as the ferrihydrite-hematite mixtures suggest minimal systematic bias in the analysis. The absolute abundances of crystalline phases when ferrihydrite is present should thus also be considered semi-quantitative. The relative abundances of crystalline phases, however, remain quantitative.

Analysis of EXAFS Spectra of Zn Incorporated in and Adsorbed to Hematite

The synthesis and characterization of Zn-substituted hematite was previously described (Frierdich and Catalano, 2012). In that prior study, fitting a single oxygen shell to the EXAFS spectrum yielded 4±1 neighbors with an interatomic distance of 1.99±0.02 Å. This appeared to suggested that zinc was tetrahedrally coordinated, but the multiple iron neighbors were consistent with zinc occupying the iron site in the structure, which is a distorted octahedron. Recent computational work (Bylaska et al., 2019) has demonstrated that zinc occupying this distorted octahedron well reproduces the observed EXAFS spectrum. In the present work, the spectrum of zinc substituted into hematite was thus fit with two oxygen shells comprised of three atoms each (Figure 7A), to reflect the distorted octahedral site in hematite. This, along with the observed iron neighbors (Table 1) is consistent with octahedral zinc occupying the distorted iron site in hematite.

The EXAFS spectrum of zinc adsorbed to hematite (Figure 7A) has more muted fine structure, consistent with a surface complex. While the coordination number for oxygen (6.2±0.5) suggests that zinc is octahedrally coordinated in this sample, the Zn-O distances is intermediate between that of tetrahedral and octahedral zinc, indicating that a mixture of species are present. The relative large σ^2 value for the shell indicates high disorder, as would be expected for a mix of four- and six-coordinated zinc. An attempt to include a second shell contribution from iron yielded a coordination number within error of zero. We attribute this to destructive interference between iron shells for inner-sphere tetrahedral and octahedral zinc species rather than indicating that zinc binds in an outer-sphere configuration.

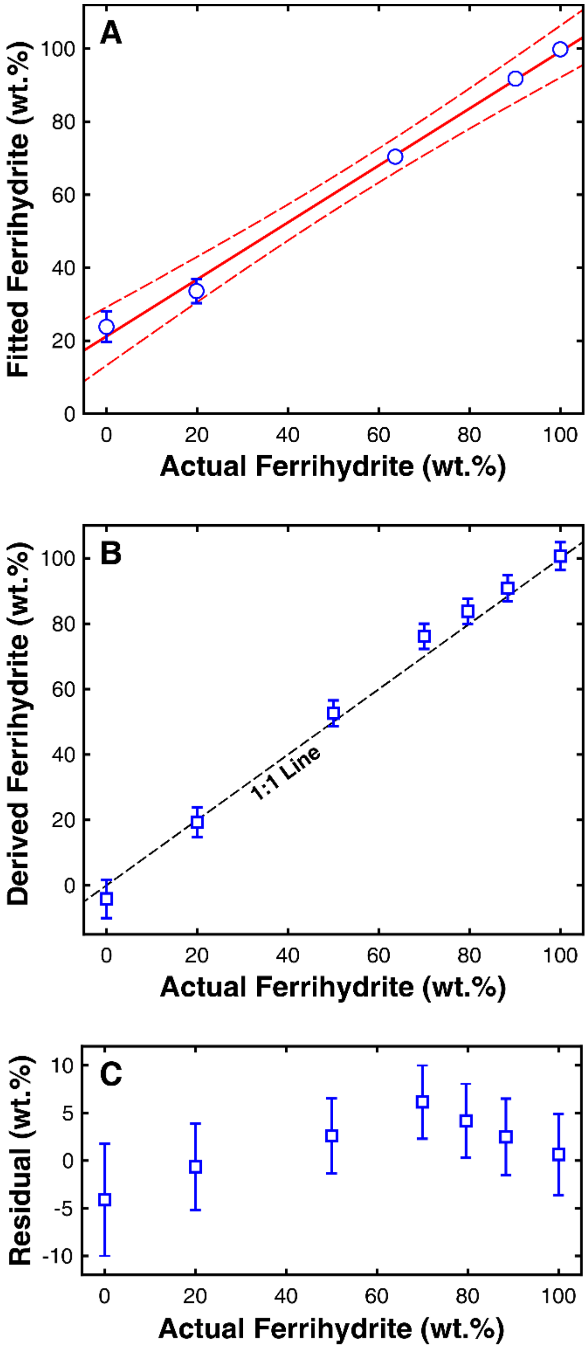

Figure S1. (A) Ferrihydrite abundances in 1:1 mixtures with zinc oxide versus actual ferrihydrite abundances. Error bars represent the fitting uncertainty derived from Rietveld refinement; data without errors have uncertainties smaller than the symbol. Also shown is the linear regression line and 95% confidence intervals. (B) Abundances of ferrihydrite in 1:1 mixtures with hematite derived from Rietveld refinement using the empirical calibration curve obtained from zinc oxide mixtures compared to actual abundances. Error bars account for both uncertainties obtained from Rietveld refinement and in the calibration curve. (C) Residual values representing the difference between derived and actual ferrihydrite abundances in mixtures with hematite.

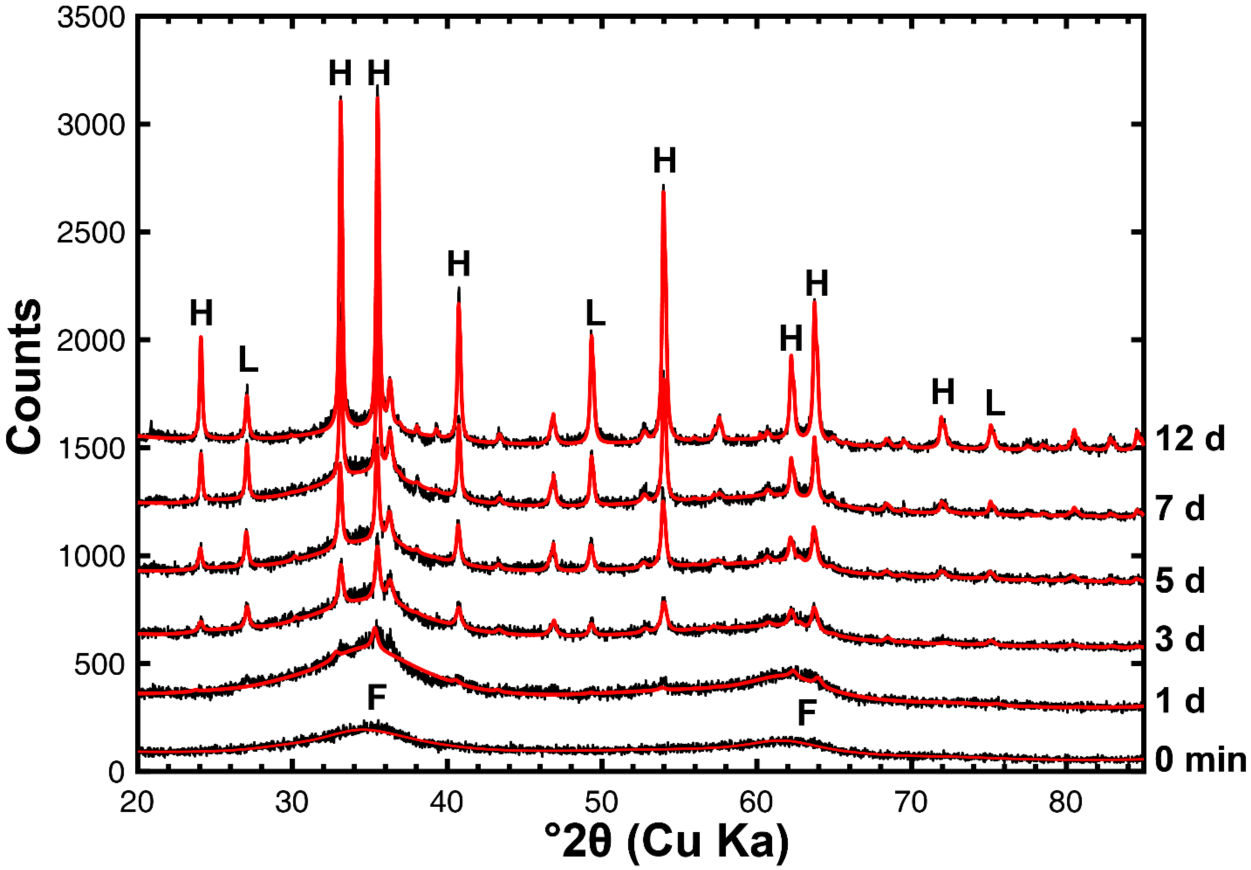

Figure S2. Rietveld refinement fit of XRD data (red) and XRD data (black) of mineral composition changed over time during 12-day Zn-ferrihydrite transformation experiment in 0.2 mM Fe(II)

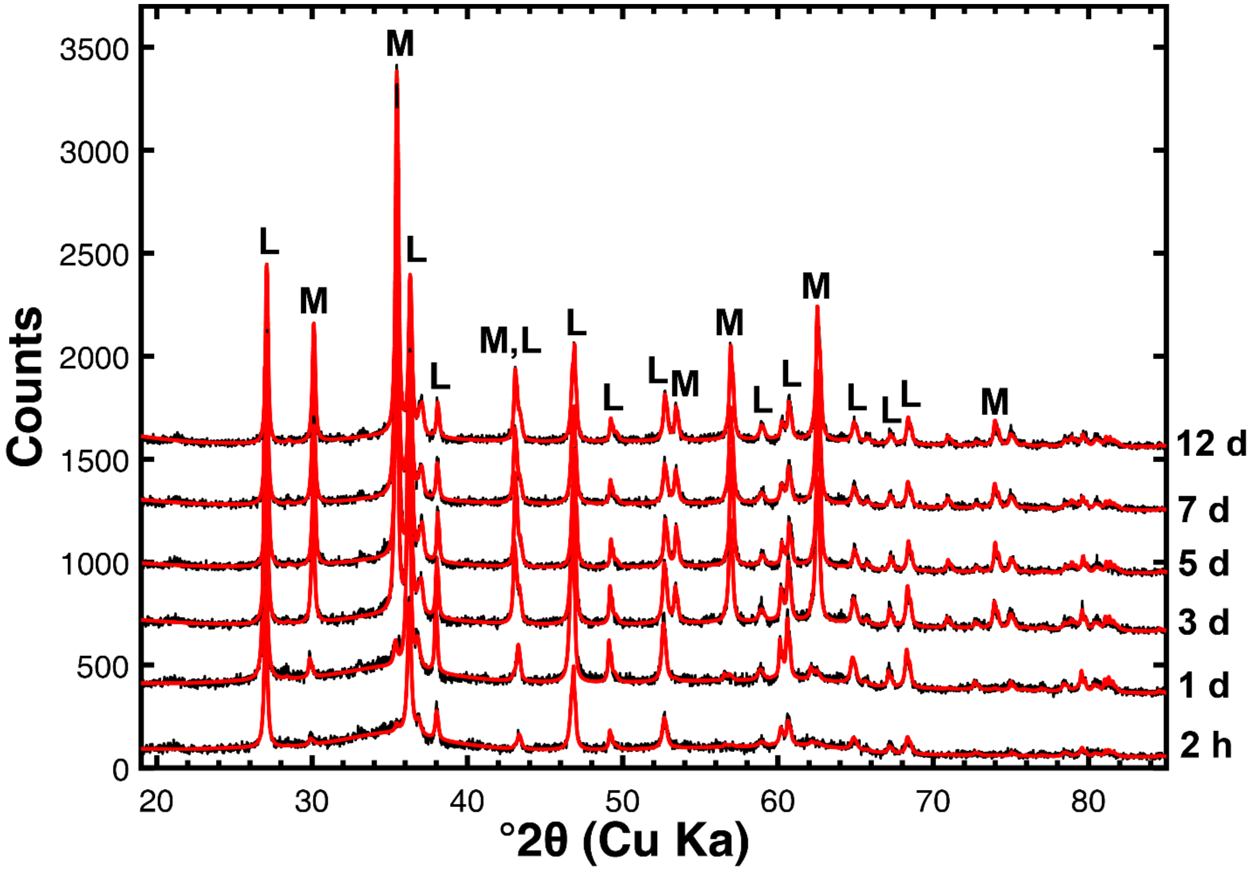

Figure S3. Rietveld refinement fit of XRD data (red) and XRD data (black) of mineral composition changed over time during 12-day Zn-ferrihydrite transformation experiment in 1.0 mM Fe(II)

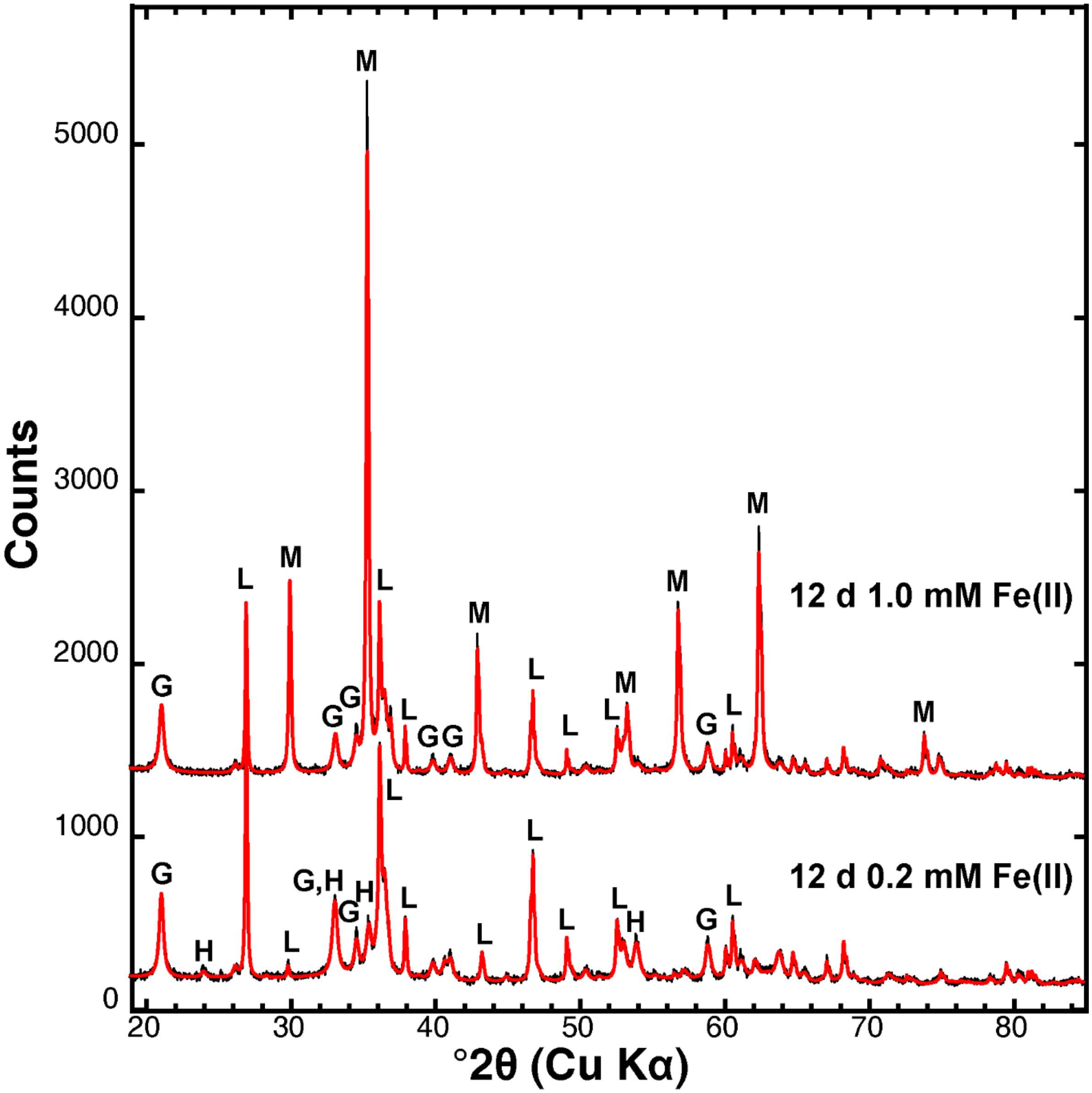

Figure S4. Rietveld refinement fit of XRD data (red) and XRD data (black) of mineral composition of the control experiments using Zn-free ferrihydrite.

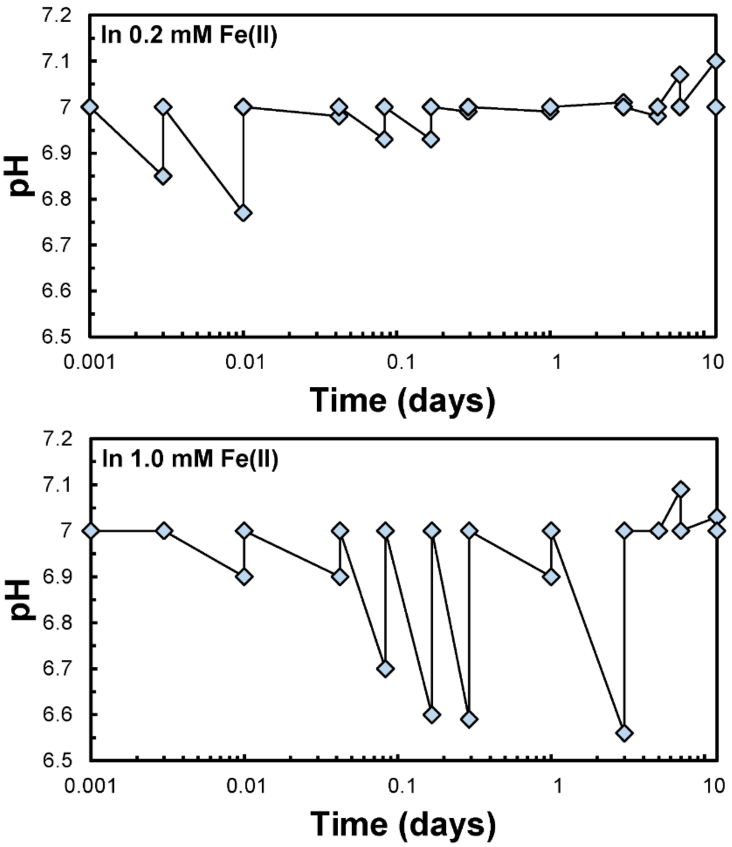

Figure S5. Drift in the pH during Zn-ferrihydrite transformation induced by 0.2 mM or 1.0 mM Fe(II). At each sampling point the pH was adjusted back to 7.0±0.1 by dropwise addition of 0.1 M NaOH

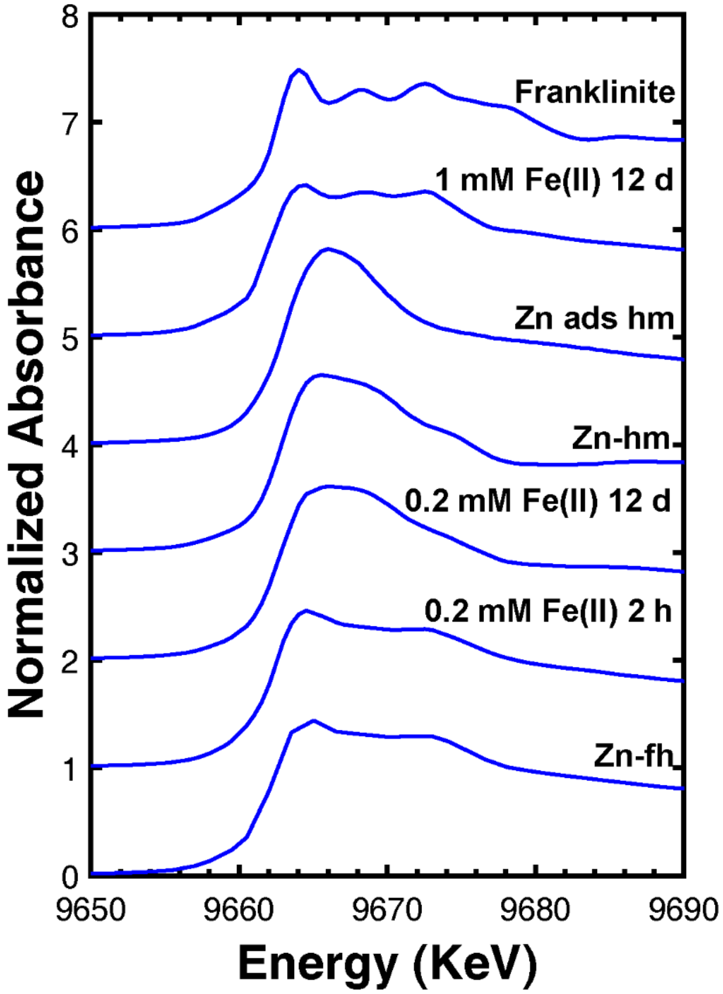

Figure S6. Zn K-edge XANES spectra of Zn-ferrihydrite (Zn-fh), Zn-ferrihydrite reacted with 0.2 mM Fe(II) for 2 hours and 12 days, standards of Zn incorporated in (Zn-hm) and adsorbed on (Zn ads hm) hematite, Zn-ferrihydrite reacted with 1.0 mM Fe(II) for 12 days, and franklinite.

Table S1. parameters from Rietveld refinement of the XRD data and the mineral abundances after recalibration using the empirical ferrihydrite parameterization.

Time	**Rietveld Refinement Results**									**Recalibrated Abundances**				
	Fh (wt.%)	Hem (wt.%)	Lep (wt.%)	Mag (wt.%)	Goe (wt.%)	R_{wp} (%)	R_{exp} (%)	χ^2		Fh (wt.%)	Hem (wt.%)	Lep (wt.%)	Mag (wt.%)	Goe (wt.%)
0.2 mM Fe(II)														
1 d	97.9±0.2	2.1±0.2	-	-	-	8.86	7.32	1.47		98±4	2.1±0.4	-	-	-
3 d	90.0±0.5	7.8±0.4	1.8±0.2	0.4±0.1	-	8.86	7.84	1.28		90±4	8±1	1.8±0.6	0.4±0.2	-
5 d	87.6±0.4	9.2±0.4	2.8±0.2	0.5±0.1		9.26	7.80	1.41		87±4	9±1	2.8±0.7	0.5±0.3	-
7 d	85.4±0.4	11.6±0.2	3.0±0.2	-	-	9.13	7.51	1.48		85±4	11.9±0.7	3.1±0.7	-	-
12 d	59.5±0.9	36.0±0.7	4.6±0.3	-	-	9.65	7.50	1.66		55±5	40±3	5±1	-	-
Control	29.6±1.6	16.3±0.7	28.7±0.7	-	25.4±0.8	9.41	7.91	1.42		13±8	20±3	35±2	-	31±3
1.0 mM Fe(II)														
2 h	80.7±0.5	-	18.7±0.5	0.6±0.1	-	11.12	9.35	1.41		80±4	-	20±2	0.6±0.2	-
1 d	64.6±0.8	-	33.8±0.8	1.6±0.1	-	10.64	8.09	1.73		61±5	-	37±3	1.7±0.3	-
3 d	48.5±1.0	-	29.3±0.6	22.2±0.5	-	10.45	8.05	1.69		41±5	-	34±2	26±2	-
5 d	47.6±1.1	-	25.6±0.6	26.8±0.6	-	11.66	8.86	1.73		39±6	-	30±2	31±2	-
7 d	41.7±1.4	-	28.2±0.8	30.1±0.8	-	11.74	8.90	1.74		31±7	-	33±3	36±3	-
12 d	45.2±1.4	-	27.3±0.8	27.5±0.7	-	12.85	8.78	2.14		36±7	-	32±3	32±3	-
Control	16.9±1.9	-	17.2±0.5	41.2±0.9	24.7±0.7	10.20	7.89	1.67		0±9	-	21±2	50±3	30±3

*Mineral labels: ferrihydrite = Fh, hematite = Hem, lepidocrocite = Lep, magnetite = Mag, goethite = Goe.

REFERENCES

Bylaska E. J., Catalano J. G., Mergelsberg S. T., Saslow S. A., Qafoku O., Prange M. P. and Ilton E. S. (2019) Association of Defects and Zinc in Hematite. *Environ. Sci. Technol.* **53**, 13687–13694.

Frierdich A. J. and Catalano J. G. (2012) Controls on Fe(II)-activated trace element release from goethite and hematite. *Environ. Sci. Technol.* **46**, 1519–1526.

Michel F. M., Ehm L., Antao S. M., Lee P. L., Chupas P. J., Liu G., Strongin D. R., Schoonen M. A. A., Phillips B. L. and Parise J. B. (2007) The structure of ferrihydrite, a nanocrystalline material. *Science.* **316**, 1726–1729.